


Vector field solution for Brinkman equation in presence of disconnected spheres

Bo Liu^{}* and S. Bhattacharya

Department of Mechanical Engineering, Texas Tech University, Lubbock, Texas 79409, USA



(Received 21 June 2020; accepted 28 September 2020; published 16 October 2020)

This paper describes the solution of a vector function around disconnected spheres where the fields are governed by a hybrid between Stokes and Helmholtz equations. The governing relation known as Brinkman equation typically appears to represent the spatial variations in Darcy's flow in porous medium as well as in unsteady Stokesian hydrodynamics. The presented analysis provides a general solution technique of the aforementioned field equation assuming inhomogeneous Dirichlet conditions at the surface of the disconnected spheres and a decaying variation at infinity. The methodology relies on the expansions in multiple sets of vector basis functions corresponding to each sphere. The key result in the formulation is the mutual transformations between the basis functions of two such sets. This allows the derivation of the matrix relations coupling the unknown amplitudes with the given inhomogeneous boundary conditions. The presented mathematical theory is validated by complementing numerical calculations. Accordingly, the solution is constructed using the outlined method, and the error in the form of departure from the intended boundary condition is evaluated. This error vanishes very quickly with increasing number of basis solutions demonstrating high accuracy and exponential spectral convergence of the numerical scheme. The versatility of the method is also demonstrated by describing the flows under both steady and unsteady conditions around particles moving in porous and liquid medium, respectively.

DOI: [10.1103/PhysRevFluids.5.104303](https://doi.org/10.1103/PhysRevFluids.5.104303)

I. INTRODUCTION

The spatial variation in a vector field corresponding to many complex systems is often described by Brinkman equation [1]. It is a hybrid between the Stokes and the Helmholtz equations, where the spatial dependence of a solenoidal vector \mathbf{v} is affected by the gradient of a scalar field p . Accordingly, the governing field equations assume the following form:

$$-\nabla p + \nabla^2 \mathbf{v} = k^2 \mathbf{v}, \quad \nabla \cdot \mathbf{v} = 0, \quad (1)$$

where both \mathbf{v} and p are treated as the dependent variables with wave number k being a constant. In absence of p , the first of the relations coincides with Helmholtz equation. In contrast, for $k=0$, the pair of equalities in Eq. (1) represent Stokes equation.

In contemporary research, Brinkman equation is receiving a significant attention. Its renewed relevance is due to the study of hitherto unexplored complicated phenomenon or complex systems. For example, analysis of inherently unsteady mutual interactions between two Brownian particles for nanofluidic [2–5] or microrheological [6–8] predictions requires consideration of Brinkman equation. Similarly, the governing equation for flow simulations through porous materials is

*bo.liu@ttu.edu

represented by Eq. (1) [9,10]. Moreover, the same can be relevant in unsteady viscoelasticity [11] or electrodynamics [12] problems.

In this paper, we provide a mathematical formulation to solve Brinkman equation, where the value of \mathbf{v} is given at the surface of two or three neighboring spheres. Apart from the spherical objects, the space is freely expanded implying a decaying \mathbf{v} and p far away from these bodies. The solution-technique can be viewed as a generalization of Many-body Stokesian dynamics [13–20], though the proposed approach has wider scopes and more versatile context beside fluid mechanics.

Our findings would be immediately applicable in modeling thermal properties of dense nanofluids where heat conductivity enhances considerably due to hydrodynamically interacting Brownian particles [3]. These suspended bodies undergoing random motion drag fluid along, and act as numerous stirrers causing an increase in heat transfer rate. In Brownian dynamics, timescale for temporal variation matches with viscous relaxation. Thus, effect of particulate motion on stochastic mass transfer can only be accounted for if inertia-corrected unsteady Stokes equation is considered. The key step in the mathematical formulation remains the solution of Brinkman equation which appears when unsteady Stokes equation is Fourier transformed from temporal to frequency space. The many-body problem addressed in this paper would represent pairwise interactions between moving bodies and reveal the cumulative impact of their motions on thermal transport [21–24].

Similar studies of Brownian dynamics are also useful in microrheological applications. In microrheology, the root-mean-square (RMS) displacement of a Brownian particle in a linearly viscoelastic fluid is recorded as function of time, and then the viscoelasticity or complex viscosity of the fluid is retrieved from the data [25]. This procedure is especially applicable to measure properties of precious samples which can be destroyed if subjected to the stresses created by a conventional rheometer. Microrheological predictions require solutions for inertia-corrected unsteady Stokes equation to calculate viscoelastic stresses. To this end, the Brinkman equation obtained from temporal Fourier transform is ultimately solved to derive the frequency-dependent mobility. The experimental results are compared with the theoretical estimation to determine the rheological constants as function of frequency. The many-body problem addressed here would suggest how to correct the error introduced by any neighboring bodies [26], as many of these are often present in the test liquid.

Furthermore, the multisphere solution of Brinkman equation can also help to calculate the effective permeability of inhomogeneous porous medium with permeable matrix and impermeable obstacles [27,28]. Many filters are constituted by such materials where multicomponent interior causes an effective filtration of suspended solutes with different sizes. The fluid velocity through this medium can be modeled by Brinkman equation in a domain with a number of no-slip nonporous obstacles. The solution technique developed in this article can be directly imported in such flow simulation. At present, the similar problems are addressed by methodologies derived from Stokesian dynamics [10] and lattice Boltzmann [29,30]. The proposed scheme builds on the existing ones enhancing the computational accuracy substantially without incurring significant cost.

In our analysis of the many-sphere system, we expand \mathbf{v} in different sets of vector basis functions of Eq. (1) corresponding to each sphere. The most crucial result in our derivation is the mutual transformations between the basis functions of these two sets. This allows us to cast the boundary conditions in terms of matrix relations coupling the unknown amplitudes with given values of \mathbf{v} at the surface of the sphere. The presented mathematical theory is validated by complementing numerical calculations that reveal diminishing errors with exponential convergence as the number of basis functions is increased.

Accordingly, the article is organized in the following way. In Sec. II, the solution-technique is outlined in such a way that it not only describes how to solve the specific two- or three-body problems, but also elucidates how to generalize it for a different system. In Sec. III, the scheme is validated by comparing computed hydrodynamic frictions with their known values and by demonstrating the decay of the error in the form of departure from the intended boundary condition with increasing number of basis solutions. The versatility of the method is illustrated in Sec. IV by constructing the velocity field in a porous medium around two impermeable spheres as well as in

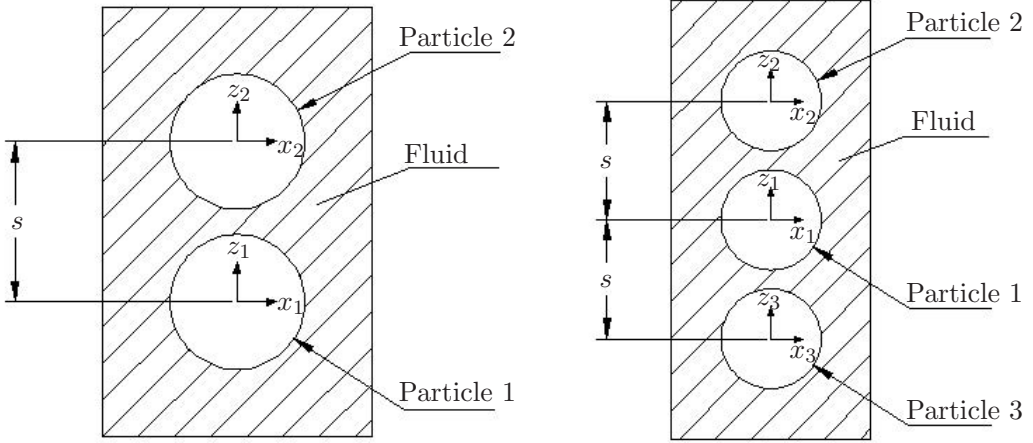


FIG. 1. Schematic diagram of a two-sphere system and a three-sphere system.

viscous liquid between two oscillating particles. The article is summarized, and the conclusions are drawn in Sec. V. The key derivations of two types of transformation coefficients are provided in two accompanying appendices.

II. SOLUTION METHODOLOGY BASED ON BASIS FUNCTION EXPANSION

In our analysis, we primarily solve Eq. (1) in an unbounded domain where two spheres of radius a_1 and a_2 have s as their center-to-center separation. The method is also extended to three-sphere systems in one specific simulation. The center of the i th particle is situated at $\mathbf{r} = \mathbf{x}_i$ with \mathbf{r} being position vector from a chosen origin. This obviously suggests that $s = |\mathbf{x}_1 - \mathbf{x}_2|$ has to be greater than $(a_1 + a_2)$. The entire formulation is considered in nondimensional form assuming that the appropriate length scale for the space is available to normalize all relevant dimensions. Hence, a_1 , a_2 , and s are treated as dimension-less quantities. The considered systems are described schematically in Fig. 1.

Accordingly, the parameter k defined in Eq. (1) is interpreted as nondimensional wave number. In general, it may be complex depending on the nature of the problem. For example, in unsteady Stokes problem, $\gamma = k^2$ would have a purely imaginary value making k a complex number with phase angle $\pi/4$. In contrast, for steady flow in porous medium, γ is a positive definite quantity so that k becomes real. For unsteady porous system, γ itself is a complex number leading to complicated phase angle for k . Keeping in mind such versatile possibilities, our analysis considers both real and imaginary values for γ .

The inhomogeneous Dirichlet boundary conditions at the the surface of two spheres complement the governing equation in Eq. (1) completing the problem statement. The solution technique is developed to accommodate any such boundary condition. Thus, we consider

$$@\mathbf{r} = \mathbf{x}_i + a_i \hat{\mathbf{e}}_r^i, \quad \mathbf{v} = \mathbf{v}_i(\theta_i, \phi_i), \quad (2)$$

where \mathbf{v}_i is a given vector function of spherical angles θ_i and ϕ_i around the center of the i th sphere situated at position vector \mathbf{x}_i . The unit normal vector in the radial direction of the i th sphere is $\hat{\mathbf{e}}_r^i$. Our numerical scheme accounts for any arbitrary but known \mathbf{v}_i .

A. General field solution in terms of vector basis functions

The linearity of Eq. (1) implies that \mathbf{v} can be expanded as the linear combination of appropriate basis functions. The challenge is to identify these functions to form the complete set corresponding to the problem of interest.

To address this issue, first we focus on the complete set of spherical basis functions $\mathbf{v}_{lms}^{i\pm}$ centered around an isolated i th sphere in free space, so that

$$\mathbf{v}_{lms}^{i\pm} = \mathbf{v}_{lms}^{\pm}(\mathbf{r} - \mathbf{x}_i). \quad (3)$$

This means that $\mathbf{v}_{lms}^{i\pm}$ can be expressed in terms of the spherical coordinates centered around the point $\mathbf{r} = \mathbf{x}_i$ which is the location of the center of the i th particle.

The vector functions \mathbf{v}_{lms}^{\pm} in Eq. (3) are solutions of Brinkman equation whose translational invariance ensures unique \mathbf{v}_{lms}^{\pm} irrespective of \mathbf{x}_i . The superscript “+” in \mathbf{v}_{lms}^{\pm} stands for regular solutions which are finite at the origin of the local spherical coordinates, but diverge far from the center. In contrast, superscript “−” denotes singular functions with singularity at the origin and decaying nature at infinity. The subscripts l and m in \mathbf{v}_{lms}^{\pm} are the eigen indices corresponding to spherical harmonics. The third index s can assume three values, 1 or 2 or 3 representing three linearly independent vectors to form the complete set of basis in 3D space. These are akin to three independent potential, vortical and pressure solutions for Stokes equation proposed by Lamb. For Brinkman equation, we derive them as

$$\mathbf{v}_{lm1}^{\pm}(\mathbf{r}_i) = \mathbf{r}_i \times \nabla \psi_{lm}^{h\pm}(\mathbf{r}_i), \quad \mathbf{v}_{lm2}^{\pm}(\mathbf{r}_i) = \nabla \times \mathbf{v}_{lm1}^{\pm}(\mathbf{r}_i), \quad \mathbf{v}_{lm3}^{\pm}(\mathbf{r}_i) = \nabla \psi_{lm}^{Pl\pm}(\mathbf{r}_i), \quad (4)$$

where $\mathbf{r}_i = \mathbf{r} - \mathbf{x}_i$ and

$$\psi_{lm}^{Pl+}(\mathbf{r}_i) = r_i^l Y_{lm}, \quad \psi_{lm}^{Pl-}(\mathbf{r}_i) = r_i^{-l-1} Y_{lm}, \quad \psi_{lm}^{h+}(\mathbf{r}_i) = \frac{g_l^+(r_i)}{r_i} Y_{lm}, \quad \psi_{lm}^{h-}(\mathbf{r}_i) = \frac{g_l^-(r_i)}{r_i} Y_{lm}, \quad (5)$$

with Y_{lm} being the normalized spherical harmonics of order l and m . The index $l = 1, 2, 3 \dots$ is related to the Legendre polynomial revealing variations along longitudes, whereas $m = 0, \pm 1, \pm 2, \dots, \pm l$ are the wave number along the latitudes. The functions g_l^{\pm} are constructed from the following recurrence relation:

$$g_l^{\pm}(r_i) = r_i \frac{d}{dr_i} [g_{l-1}^{\pm}(r_i)/r_i], \quad (6)$$

starting from the initial ones: $g_0^+(r_i) = \sinh(kr_i)$ and $g_0^-(r_i) = \exp(-kr_i)$. Here, r_i , θ_i , and ϕ_i are considered as the spherical coordinates centered around the point $\mathbf{r} = \mathbf{x}_i$. The regularity of \mathbf{v}_{lms}^+ is enforced by $g_0^+(r_i) = \sinh(kr_i)$, because it remains finite at $r_i = 0$ with continuous derivatives of arbitrary order even after a division by r_i . Likewise, the required decaying feature in \mathbf{v}_{lms}^- at infinity is assured by the exponential decrease in all derivatives of arbitrary order involving $g_0^-(r_i) = \exp(-kr_i)$.

The general solution for \mathbf{v} in presence of multiple spheres can be formed by pondering on two facts. First, the existence of each sphere excludes its volume from the domain allowing possible singularities at its center. These singular solutions cannot be represented by any regular functions or singularities at a different location. Second, any regular solution \mathbf{v}_{lms}^{i+} centered around one point can be expressed as the linear combination of $\mathbf{v}_{lms}^{j\pm}$ with $i \neq j$. Accordingly, we conclude that \mathbf{v} can be expanded as the linear combinations of all the singular functions corresponding to every sphere and any one of the regular sets associated to one of the spheres:

$$\mathbf{v} = \sum_{lmsi} \alpha_{lmsi}^{i-} \mathbf{v}_{lms}^{i-} + \sum_{lms} \alpha_{lms}^{1+} \mathbf{v}_{lms}^{1+} = \sum_{lmsi} \alpha_{lmsi}^{i-} \mathbf{v}_{lms}^{i-} + \sum_{lms} \alpha_{lms}^{2+} \mathbf{v}_{lms}^{2+} = \dots \quad (7)$$

For unbounded space in absence of any confining boundaries, however, regular solutions cannot be present in the expansion. Thus, for spheres in unbounded domain, we conclude

$$\mathbf{v} = \sum_{lmsi} \alpha_{lms}^{i-} \mathbf{v}_{lms}^{i-}, \quad (8)$$

assuming all α_{lms}^{j+} are identically zero.

Thus, solution for \mathbf{v} would be completely known if the unknown amplitudes α_{lms}^{i-} are evaluated. The focus of the subsequent analysis would be to achieve this by exploiting the boundary conditions. The presented formulation is general so far for any many-body system with arbitrary number of spheres. For our two-body problem, we need to only consider two values of i with 1 for the first sphere and 2 for the second one.

B. Matrix representation for unknown amplitudes

The unknown amplitudes α_{lms}^{i-} are evaluated by forming a matrix representation coupling α_{lms}^{i-} with given boundary conditions involving known \mathbf{v}_i . This matrix relation can be conveniently constructed due to three simple observations.

The first convenient feature of the basis vectors $\mathbf{v}_{lms}^{i\pm}$ is that these are separable functions in the spherical coordinates corresponding to the i th particle. This implies that the dependence of $\mathbf{v}_{lms}^{i\pm}$ on radius r_i and spherical angles θ_i, ϕ_i can be factorized:

$$\mathbf{v}_{lms}^{i\pm} = \sum_{\sigma} [f_{lms\sigma}^{\pm}(r_i) \hat{\mathbf{e}}_{lms}^i(\theta_i, \phi_i)]. \quad (9)$$

Here, the index σ assumes three values 1, 2, 3 making angle-dependent $\hat{\mathbf{e}}_{lms}^i$ a complete set of basis for 3D vector space. These vectors are

$$\hat{\mathbf{e}}_{lm1}^i = \mathbf{r}_i \times \nabla Y_{lm}, \quad \hat{\mathbf{e}}_{lm2}^i = \hat{\mathbf{e}}_{r_i} Y_{lm}, \quad \hat{\mathbf{e}}_{lm3}^i = r_i \nabla Y_{lm}, \quad (10)$$

which not only span 3D physical space but also account for all possible variations on a spherical surface in functional space. Recasting Eqs. (4) and (5) in Eq. (9) we recognize

$$\begin{aligned} \mathbf{v}_{lm1}^{i\pm} &= \frac{g_l^{\pm}(r_i)}{r_i} \hat{\mathbf{e}}_{lm1}^i, \quad \mathbf{v}_{lm2}^{i\pm} = -\frac{l(l+1)}{r_i^2} g_l^{\pm}(r_i) \hat{\mathbf{e}}_{lm2}^i - \frac{g_l^{\pm'}(r_i)}{r_i} \hat{\mathbf{e}}_{lm3}^i, \\ \mathbf{v}_{lm3}^{i+} &= l r_i^{l-1} \hat{\mathbf{e}}_{lm2}^i + r_i^{l-1} \hat{\mathbf{e}}_{lm3}^i, \quad \mathbf{v}_{lm3}^{i-} = (-l-1) r_i^{-l-2} \hat{\mathbf{e}}_{lm2}^i + r_i^{-l-2} \hat{\mathbf{e}}_{lm3}^i. \end{aligned} \quad (11)$$

The scalar functions $f_{lms\sigma}^{\pm}$ can be conveniently arranged in a 3×3 matrix $[\mathbf{F}_{lm}^{\pm}]$,

$$[\mathbf{F}_{lm}^+] = \begin{bmatrix} \frac{g_l^+(r_i)}{r_i} & 0 & 0 \\ 0 & -\frac{l(l+1)}{r_i^2} g_l^+(r_i) & -\frac{g_l^{+'}(r_i)}{r_i} \\ 0 & l r_i^{l-1} & r_i^{l-1} \end{bmatrix}, \quad [\mathbf{F}_{lm}^-] = \begin{bmatrix} \frac{g_l^-(r_i)}{r_i} & 0 & 0 \\ 0 & -\frac{l(l+1)}{r_i^2} g_l^-(r_i) & -\frac{g_l^{-'}(r_i)}{r_i} \\ 0 & (-l-1) r_i^{-l-2} & r_i^{-l-2} \end{bmatrix}, \quad (12)$$

as the σ th element in the s th row. Crucially, $[\mathbf{F}_{lm}^{\pm}]$ only depend on radial coordinates r_i .

The second feature useful in construction of the matrix relation is that any vector function like $\mathbf{v}_i(\theta_i, \phi_i)$ on the i th spherical surface can be expanded as a linear combination of $\hat{\mathbf{e}}_{lms}^i$:

$$\mathbf{v}_i(\theta_i, \phi_i) = \sum_{lms} [a_{lms}^i \hat{\mathbf{e}}_{lms}^i]. \quad (13)$$

Here, a_{lms}^i are constants which are treated as known quantities for given \mathbf{v}_i .

Third and finally, all basis functions in the set for one particle can be expressed always as a linear combination of the basis vectors for another. If the original function is singular, then the validity of

such equality would depend on the radius of convergence. Hence, one concludes

$$\mathbf{v}_{lms}^{i-} = \sum_{l'm's'} [M_{lmsl'm's'}^{ij=} \mathbf{v}_{l'm's'}^{j-}], \quad (14)$$

for $|\mathbf{r} - \mathbf{x}_j| > |\mathbf{x}_i - \mathbf{x}_j|$. More importantly, we can also claim

$$\mathbf{v}_{lms}^{i-} = \sum_{l'm's'} [M_{lmsl'm's'}^{ij\mp} \mathbf{v}_{l'm's'}^{j+}], \quad (15)$$

for $|\mathbf{r} - \mathbf{x}_j| < |\mathbf{x}_i - \mathbf{x}_j|$. The relation in Eq. (15) allows us to cast the boundary conditions in a matrix equation relating unknown amplitudes of singularities α_{lms}^{i-} to known constants a_{lms}^i .

Thus, for an N -sphere system with L number of singular basis, $N * L$ number of unknown amplitudes are mutually coupled in exact same number of linear relations which the matrix would ultimately represent. For two-particle system, Eq. (15) is first used to replace \mathbf{v}_{lms}^{2-} in Eq. (8) in terms of \mathbf{v}_{lms}^{1+} . Then, the boundary condition at the surface of the first sphere becomes

$$a_{\lambda\mu\sigma}^1 = \sum_s [\alpha_{\lambda\mu s}^{1-} f_{\lambda\mu s}^-(a_1)] + \sum_{lms'} [\alpha_{lms}^{2-} M_{lms\lambda\mu s'}^{21\mp} f_{\lambda\mu s'\sigma}^+(a_1)]. \quad (16)$$

Also, substituting \mathbf{v}_{lms}^{1-} with \mathbf{v}_{lms}^{2+} in Eq. (8) recasts the boundary condition at the second sphere,

$$a_{\lambda\mu\sigma}^2 = \sum_s [\alpha_{\lambda\mu s}^{2-} f_{\lambda\mu s}^-(a_2)] + \sum_{lms'} [\alpha_{lms}^{1-} M_{lms\lambda\mu s'}^{12\mp} f_{\lambda\mu s'\sigma}^+(a_2)]. \quad (17)$$

The coupled relations in Eqs. (16) and (17) can be concisely described by assuming a row matrix $\langle \mathbf{a} |$ with elements $a_{\lambda\mu\sigma}^1$ and $a_{\lambda\mu\sigma}^2$ as well as another one $\langle \alpha |$ containing α_{lms}^{1-} and α_{lms}^{2-} . In all matrices, the elements corresponding to each spheres are stacked together so that the respective subsets are displayed as subrows

$$\langle \mathbf{a} | = \langle \{a_{\lambda\mu\sigma}^1\}, \{a_{\lambda\mu\sigma}^2\} |, \quad \langle \alpha | = \langle \{\alpha_{lms}^{1-}\}, \{\alpha_{lms}^{2-}\} |. \quad (18)$$

The consequent matrix relation representing both Eqs. (16) and (17) becomes

$$\langle \mathbf{a} | = \langle \alpha | [\mathbf{G}]. \quad (19)$$

The square matrix $[\mathbf{G}]$ is the grand mobility matrix with the following substructures:

$$[\mathbf{G}] = \begin{bmatrix} [F_1^-] & [M_{12}^\mp][F_2^+] \\ [M_{21}^\mp][F_1^+] & [F_2^-] \end{bmatrix}. \quad (20)$$

Submatrix $[F_i^\pm]$ has $f_{\lambda\mu s}^\pm(a_i)$ as its only nonzero elements arranged in 3×3 diagonal blocks formed due to three values of s and σ , while $[M_{ij}^\mp]$ contains transformation coefficients $M_{lms\lambda\mu s'}^{ij\mp}$. For three or more spheres, $[\mathbf{G}]$ can be built similarly by using $[F_i^-]$ for i th sphere as the i th diagonal block and $[M_{ij}^\mp][F_j^+]$ for i, j th pair as the i, j th off-diagonal block.

C. Expressions of transformation coefficients

The most nontrivial step in our analysis is derivation of the transformation coefficients $M_{lms\lambda\mu s'}^{ij\mp}$ or construction of submatrix $[M_{ij}^\mp]$ in Eq. (20). The details of this analysis is described in the Appendix, where its generality indicates that the same approach can solve different linear field equations in other problems. In this subsection, however, we only outline the final expressions for $[M_{ij}^\mp]$ relevant in the numerical implementation of the solution scheme.

In reality, $[M_{ij}^\mp]$ is a two-body quantity even for $N > 2$. So we exploit the inherent symmetry in two-sphere system by defining the line joining the centers as the z axis of a cylindrical coordinate so that the geometry becomes axi-symmetric with $\mathbf{x}_1 - \mathbf{x}_2 = s\hat{\mathbf{e}}_z$. The axial symmetry is retained even in our three-body simulation by placing the spheres colinearly. It makes the matrix relation Eq. (19)

block-diagonalized in m and μ meaning that the elements of $[\mathbf{G}]$ are identically 0 if $m \neq \mu$. Then, we need to only find $M_{lms\lambda\mu s'}^{ij\mp}$ for specific values of same m and μ . Moreover, if \mathbf{v}_i is induced by pure translations and rotations, then only three m or μ remain relevant where either $m = \mu = 0$, or $m = \mu = \pm 1$. Thus, we can assert

$$M_{lms\lambda\mu s'}^{ij\mp} = M_{ls\lambda s'}^{ijm\mp} \delta_{m\mu}, \quad (21)$$

so that the nonzero $M_{ls\lambda s'}^{ijm\mp}$ can be concisely stacked in a matrix $[M_m^{ij\mp}]$. It is created with nine square submatrices in an 3×3 arrangement with each subblock corresponding to specific values of s and s' . However, the elements of the submatrices represent different l and λ . More specifically, as $s = 1, 2, 3$ and $s' = 1, 2, 3$, all elements of the submatrix at the location $q-q'$ in the 3×3 structure would have $s = q$ and $s' = q'$. Then also, the $v-v'$ location within the subblock for a specific element would relate it to $l = |m| + v - 1$ and $\lambda = |m| + v' - 1$.

The derivation elaborated in the Appendix is summarized to infer that

$$[M_m^{12\mp}] = \begin{bmatrix} [H_m] + s[H_m][R_m] & s[H_m][C_m] & 0 \\ -k^2 s[H_m][C_m] & [H_m] + s[H_m][R_m] & 0 \\ 0 & 0 & [P_m] \end{bmatrix}. \quad (22)$$

Here, the aforementioned submatrices shown in the 3×3 structure is constructed by the following way. The submatrices $[R_m]$ and $[C_m]$ have simple forms where the former is a bidiagonal sparse matrix, and the latter is a diagonal matrix. Accordingly, an element of $[R_m]$ defined as $R_{l\lambda}^m$ is given by

$$R_{l\lambda}^m = -\{(l - m + 1)/[(2l + 1)(l + 1)]\} \delta_{(l+1)\lambda} + \{(l + m)k^2/[l(2l + 1)]\} \delta_{(l-1)\lambda}, \quad (23)$$

whereas a similar component $C_{l\lambda}^m$ associated to $[C_m]$ is

$$C_{l\lambda}^m = \{im/[l(l + 1)]\} \delta_{l\lambda}. \quad (24)$$

The expressions for remaining submatrices $[H_m]$ and $[P_m]$ are more involved. These are provided for different relevant values of m sequentially below.

When $m = 0$, we derive that

$$[H_0] = [N_1^h]^{-1} [N_2^h], \quad \text{where } [N_1^h] = \begin{bmatrix} \langle e_1 | [I] \\ \langle e_1 | [T_0] \\ \langle e_1 | [T_0]^2 \\ \vdots \\ \langle e_1 | [T_0]^l \end{bmatrix}, \quad [N_2^h] = \begin{bmatrix} \langle e_1 | [T_0'] [D_h] \\ \langle e_1 | [T_0'] [D_h] [T_0] \\ \langle e_1 | [T_0'] [D_h] [T_0]^2 \\ \vdots \\ \langle e_1 | [T_0'] [D_h] [T_0]^l \end{bmatrix}. \quad (25)$$

Here, the row $\langle e_1 | = \langle 1, 0, \dots, 0 |$ has its first component to be 1 with all others being 0. Also, submatrix $[T_0]$ is a bidiagonal matrix with elements as follows:

$$T_{l\lambda}^0 = \{(l + 1)/(2l + 1)\} \delta_{(l+1)\lambda} + \{lk^2/(2l + 1)\} \delta_{(l-1)\lambda}. \quad (26)$$

In contrast, submatrix $[D_h]$ is a diagonal matrix with elements

$$D_{l\lambda}^h = \{g_l^-(s)/g_l^+(s)\} \delta_{l\lambda} \quad (27)$$

dependent on radial functions defined in Eq. (6). We numerically compute $[T_0']$ from $[T_0]$:

$$[T_0'] = \sum_{n=0}^{n_{\max}} s^n [T_0]^n / n!, \quad (28)$$

where the upper limit n_{\max} has to be considerably greater than $e * s * |k|/\sqrt{2}$ for good convergence. Similarly,

$$[P_0] = [N_1^{\text{PI}}]^{-1} [N_2^{\text{PI}}], \quad \text{where } [N_1^{\text{PI}}] = \begin{bmatrix} \langle e_1 | [I] \\ \langle e_1 | [Q_0^-] \\ \langle e_1 | [Q_0^-]^2 \\ \vdots \\ \langle e_1 | [Q_0^-]^l \end{bmatrix}, \quad [N_2^{\text{PI}}] = \begin{bmatrix} \langle e_1 | [Q_0^{-'}] [D_{\text{PI}}] \\ \langle e_1 | [Q_0^{-'}] [D_{\text{PI}}] [Q_0^+] \\ \langle e_1 | [Q_0^{-'}] [D_{\text{PI}}] [Q_0^+]^2 \\ \vdots \\ \langle e_1 | [Q_0^{-'}] [D_{\text{PI}}] [Q_0^+]^l \end{bmatrix}. \quad (29)$$

Here, submatrices $[D_{\text{PI}}]$, $[Q_0^-]$, and $[Q_0^+]$ are sparse matrices whose respective elements are

$$D_{l\lambda}^{\text{PI}} = |s|^{-2l-1} \delta_{l\lambda}, \quad Q_{l\lambda}^{0-} = -(l+1) \delta_{(l+1)\lambda}, \quad Q_{l\lambda}^{0+} = l \delta_{(l-1)\lambda}. \quad (30)$$

This makes D_{PI} a diagonal, $[Q_0^-]$ an upper-diagonal and $[Q_0^+]$ a lower-diagonal matrix. If submatrix $[Q_0^-]$ is known, then we construct

$$[Q_0^{-'}] = \sum_{n=0}^{n_{\max}} s^n [Q_0^-]^n / n!, \quad (31)$$

which becomes diagonal dominant, but nonsparse matrix.

When $m = 1$, we find

$$[H_1] = [A^h]^{-1} [N_1^h]^{-1} [N_2^h] [A^h], \quad [P_1] = [N_1^{\text{PI}}]^{-1} [N_2^{\text{PI}}] [A^{\text{PI}}]. \quad (32)$$

Here, submatrix $[A^h]$ is a bidiagonal matrix with elements $A_{l\lambda}^h$ as

$$A_{l\lambda}^h = \left(-\frac{1}{2l+1} \right) \delta_{l\lambda} + \left(\frac{k^2}{2l+1} \right) \delta_{(l-2)\lambda}, \quad (33)$$

and lower-diagonal submatirx $[A^{\text{PI}}]$ is constructed with $\delta_{(l-2)\lambda}$ as its component. In contrast, when $m = -1$,

$$[H_{-1}] = [B^h]^{-1} [N_1^h]^{-1} [N_2^h] [B^h], \quad [P_{-1}] = [B^{\text{PI}-}] [N_1^{\text{PI}}]^{-1} [N_2^{\text{PI}}] [B^{\text{PI}+}], \quad (34)$$

where bidiagonal $[B^h]$ has the same structure like $[A^h]$ so that

$$B_{l\lambda}^h = \frac{(l+1)(l+2)}{(2l+1)} \delta_{l\lambda} - \frac{l(l-1)}{(2l+1)} k^2 \delta_{(l-2)\lambda}, \quad (35)$$

and diagonal $[B^{\text{PI}-}]$ is represented by

$$B_{l\lambda}^{\text{PI}-} = -(l+1)(l+2) \delta_{l\lambda}. \quad (36)$$

Also, submatrix $[B^{\text{PI}+}]$ has elements $B_{l\lambda}^{\text{PI}+}$ as

$$B_{l\lambda}^{\text{PI}+} = -l(l-1) \delta_{(l-2)\lambda}, \quad (37)$$

which makes it lower-diagonal.

The aforementioned results enable us to construct grand mobility matrix $[G]$ after combining with $[F_i^{\pm}]$ in an appropriate way shown in Eq. (20). Thus, one can find the proper amplitudes $\alpha_{\lambda\mu s}^{i-}$ corresponding to arbitrary boundary conditions given at the surface of both spheres from Eq. (19).

III. CONVERGENCE FOR THE NUMERICAL SCHEME AND VALIDATIONS

In this section, we first briefly outline the computational implementation of the mathematical formulation. Then, we design numerical experiments to reveal the convergence feature of the scheme as well as to validate our theory.

A. Numerical implementation

We use the matrix relations derived in Sec. II to numerically solve for the vector field \mathbf{v} , when different boundary conditions are provided on the surface of the spheres. The computational scheme essentially has three steps.

In the first step, the grand mobility matrix $[\mathbf{G}]$ defined in Eq. (19) is created using the expressions described in Sec. II C. The size of the square submatrices corresponding to the indices l and λ depends on their largest value referred as l_{\max} . Ideally, l_{\max} should tend to ∞ , but the main objective of our numerical investigation is to figure out what value of l_{\max} should be taken as reasonably large. We have seen that $l_{\max}=16$ yields sufficiently accurate result even for the most difficult geometry considered in our simulation.

The second step of the algorithm is to invert the grand mobility matrix $[\mathbf{G}]$. For $l_{\max}=16$, this operation takes relatively less time than the previous task. However, if l_{\max} is increased considerably, the inversion would become the most time-consuming step, as the required time for it would scale as l_{\max}^3 in contrast to l_{\max}^2 cost for construction.

The third and final task is to identify the row $\langle \mathbf{a} |$ in Eq. (19) for the given boundary condition. The unknown amplitudes in $\langle \alpha |$ are obtained by premultiplying $\langle \mathbf{a} |$ to the inverse of $[\mathbf{G}]$.

The block-diagonalization implying $m=\mu$ for axisymmetric geometries is exploited in the last step where rows $\langle \mathbf{a} |$ and $\langle \alpha |$ are constructed. It is to be noted that matrices $[F_i^-]$ in Eq. (20) are block-diagonalized over m and μ indices with $m=\mu$ like $[M_{12}^\mp]$ as shown in Eq. (21). This means that the grand mobility matrix $[\mathbf{G}]$ also exhibits similar block-diagonalization as in Eq. (21). Hence, if we consider the following structure for two-body $[\mathbf{G}]$

$$[\mathbf{G}] = \begin{bmatrix} [G_{11}] & [G_{12}] \\ [G_{21}] & [G_{22}] \end{bmatrix}, \quad (38)$$

then an element of $[G_{ij}]$ defined as $G_{lms\lambda\mu s'}^{ij}$ is given by

$$G_{lms\lambda\mu s'}^{ij} = G_{ls\lambda s'}^{ijm} \delta_{m\mu}. \quad (39)$$

The quantities $G_{ls\lambda s'}^{ijm}$ is used to construct smaller matrices $[G_m^{ij}]$ for each value of m like the way we form $[M_m^{ij\mp}]$. Such simplification prompts us to restructure matrices $\langle \mathbf{a} |$ and $\langle \alpha |$, where the elements with same value of index m (same as μ) are grouped together as subrows $\langle \mathbf{a}_m^j |$ or $\langle \alpha_m^j |$. consequently, relations involving quantities with specific m get decoupled from those with different m yielding the following reduction:

$$\langle \langle \mathbf{a}_m^1 |, \langle \mathbf{a}_m^2 | | = \langle \langle \alpha_m^1 |, \langle \alpha_m^2 | | \begin{bmatrix} [G_m^{11}] & [G_m^{12}] \\ [G_m^{21}] & [G_m^{22}] \end{bmatrix}. \quad (40)$$

Thus, we identify element a_{ls}^{jm} of $\langle \mathbf{a}_m^j |$ for specific l and s corresponding to a boundary condition at j th sphere on z axis, and find $\langle \alpha_m^j |$ by inverting Eq. (40) for all relevant m . The outlined construction can be easily extended to axi-symmetric configuration with three or more spheres by introducing respective subblocks.

We specifically focus on the linear and angular motion of the spheres when both have centers aligned on z axis. In such geometry, translation and rotation along z axis only contribute nonzero elements in $\langle \mathbf{a}_0^j |$ causing trivial rows for $m \neq 0$. For unit rectilinear velocity along z , the only nonzero element in $\langle \mathbf{a}_0^j |$ corresponds to $l=1$ and $s=2, 3$ so that the sole nontrivial components are given by

$$a_{12}^{j0} = a_{13}^{j0} = 1. \quad (41)$$

Similarly, for unit rotational velocity, a_{ls}^{j0} ($l=1, s=1$) is the only nonzero term in $\langle \mathbf{a}_0^j |$:

$$a_{11}^{j0} = 1. \quad (42)$$

In contrast, for same geometry, translation or rotation in x - y plane only involves $\langle \mathbf{a}_{\pm 1}^j |$ implying $\langle \mathbf{a}_m^j |$ to be null row for $m \neq \pm 1$. For a linear velocity $u_x \hat{\mathbf{e}}_x + u_y \hat{\mathbf{e}}_y$ as well as an angular velocity $\omega_x \hat{\mathbf{e}}_x + \omega_y \hat{\mathbf{e}}_y$, all nontrivial elements in $\langle \mathbf{a}_{\pm 1}^j |$ with l and s values as subscripts are listed in the following two equations, respectively:

$$a_{12}^{j1} = a_{13}^{j1} = -u_x/2 + iu_y/2, \quad a_{12}^{j-1} = a_{13}^{j-1} = u_x + iu_y, \quad (43)$$

and

$$a_{11}^{j1} = -\omega_x/2 + i\omega_y/2, \quad a_{11}^{j-1} = \omega_x + i\omega_y. \quad (44)$$

The relations in Eqs. (41)–(44) provide all possible boundary conditions associated to the rigid body motion. In the same way, analogous relations can be derived for any arbitrary more complicated velocity field at spherical surfaces also.

B. Spectral convergence results for two-sphere systems

We design a number of numerical experiments to validate our methodology. Accordingly, specific geometries are assumed with given separation between two spheres, and specific boundary conditions are considered at their surfaces. Then, \mathbf{v} is computed following the steps outlined in the previous subsection for various values of the wave number k .

Our simulations consider spheres of similar size with $a_1 = a_2 = a$ where three different separation distances between their centers are chosen to create different geometries. The closest configuration has $s = 2.1 * a$ which means the surface-to-surface gap would be an order of magnitude less than the spherical dimensions. We focus on such geometry because we have seen that very small gap between two equal spheres causes most difficulties in convergence with increasing l_{\max} . In addition, $s/a = 2.25$ and $s/a = 2.5$ are also taken into account to demonstrate how convergence error decreases with increasing s .

To maximize the contrast in relative motion, we keep one of the spheres fixed with zero interfacial velocity, whereas the second one either translates or rotates. Accordingly, we investigate four different independent motions of the moving particle yielding four problems with distinct inhomogeneous boundary conditions. The first one is a normal translation with unit velocity along the z axis which is the line of symmetry joining the centers. The second motion is tangential unit linear velocity perpendicular to the line of symmetry along the x axis. The third and the fourth inhomogeneous boundary conditions on the moving sphere correspond to normal and tangential rotations along the z and x axes, respectively.

We compute the amplitudes of singularities $\langle \alpha |$ following the procedures outlined in Sec. III A for each of the four problems corresponding to four motions of the second particle. Then, Eq. (8) is used to construct the vector field \mathbf{v} . Finally, we consider a series of tests to validate our mathematical derivations and numerical methodology.

First, we use finite difference to check whether the solution from our basis expansion satisfies the governing equations in Eq. (1). The finite difference provides the Laplacian and divergence of \mathbf{v} as well as ∇p . We investigate whether $\nabla^2 \mathbf{v} - \nabla p$ and $\nabla \cdot \mathbf{v}$ approaches $k^2 \mathbf{v}$ and 0, respectively. This basic check has shown that the constructed \mathbf{v} at any arbitrary point obeys both the momentum and continuity relations in Eq. (1). It is an expected observation though, as this only verifies the correctness of the basis functions used in Eq. (8).

Our second test is more complex where we demonstrate that the outlined scheme can ensure the satisfaction of given boundary conditions at the spherical surface by constructing correct $\langle \alpha |$. To this end, we directly compute \mathbf{v} according to Eq. (8) at the interfaces, and calculate errors by subtracting it from the provided \mathbf{v} as per boundary conditions. These deviations are presented in Figs. 2–5 for the previously mentioned four motions of the second sphere. In all of these, two error norms are obtained: (1) an RMS value derived from averaging over 100 grids distributed uniformly on the spheres, (2) the maximum magnitude seen among all these points. Both are presented as functions of the spectral size defined by l_{\max} .

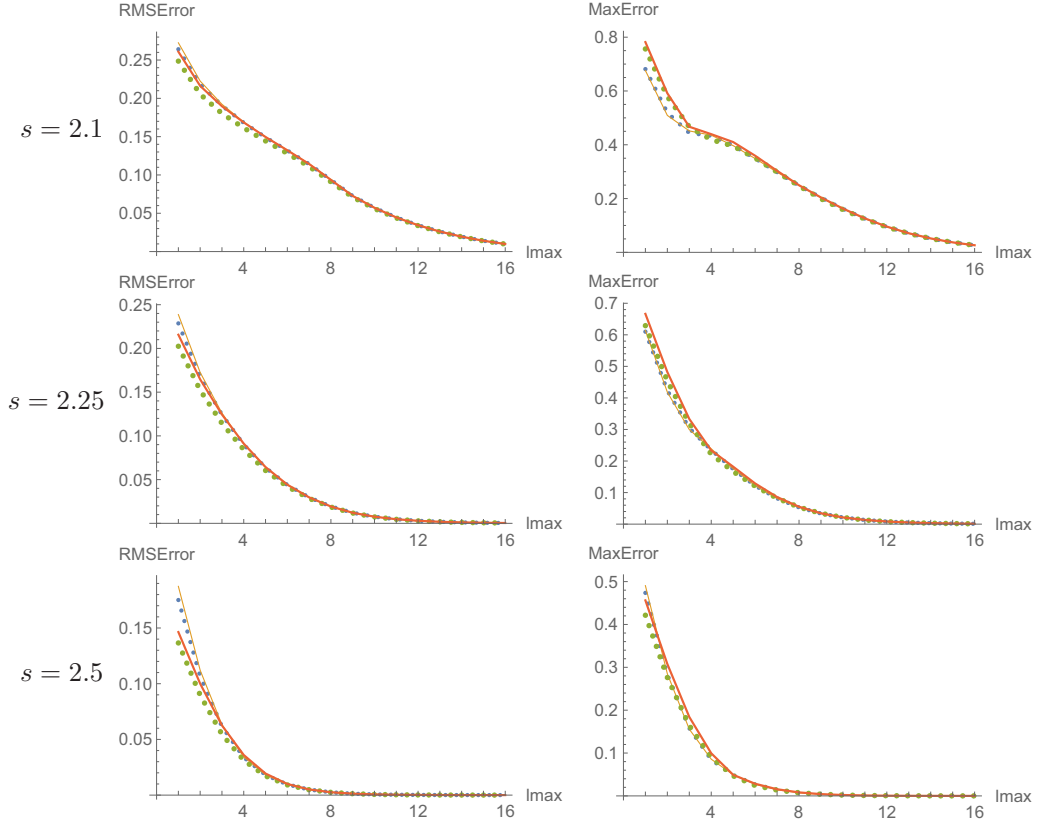


FIG. 2. Spectral convergence for normal translation along z with RMS error (left panel) and maximum error (right panel), where γ is i (thin dotted line), 1 (thin solid line), $10i$ (thick dotted line), and 10 (thick solid line). The rows represent different separations s as displayed.

We illustrate the versatility of our method by considering four different wave number k for all geometries described in Figs. 2–5. As often $k^2 = \gamma$ is the key parametric quantity in different systems, we actually assign the value of γ . Two real and two imaginary values are selected keeping in mind their relevance in inhomogeneous porous medium and unsteady Stokesian dynamics, respectively. Also, we intend to see considerable differences between our simulation and standard Stokesian computations. This is why magnitude of γ is chosen as either 1 or much greater than 1. For given γ , there should be two values of k in complex plane. The roots of k with positive real part is the one used in the simulation, as only this corresponds to physically valid solution with appropriate decay at infinity.

In Fig. 2, we simulate \mathbf{v} when the second sphere moves towards the first with a translation normal to their surface at the location of minimum separation. This means that the motion is along the z axis on which both centers reside. From steady Stokesian analysis [31–33], it is a common knowledge that such normal motions to the separating surfaces in close contact are the most difficult for proper satisfaction of boundary conditions. This is also evident for Brinkman equation according to Fig. 2. The errors are most prominent for the normal motion especially when the particles are separated by the smallest distance. Still, even the maximum error at the interface approaches to 1% for $s/a = 2.1$, when l_{\max} is 16. The same error becomes less than 0.1% when spheres are more separated.

Unidirectional relative motion tangential to the separating distance incurs less error compared to the normal translation. A tangential rectilinear or angular velocity along x or y direction produces

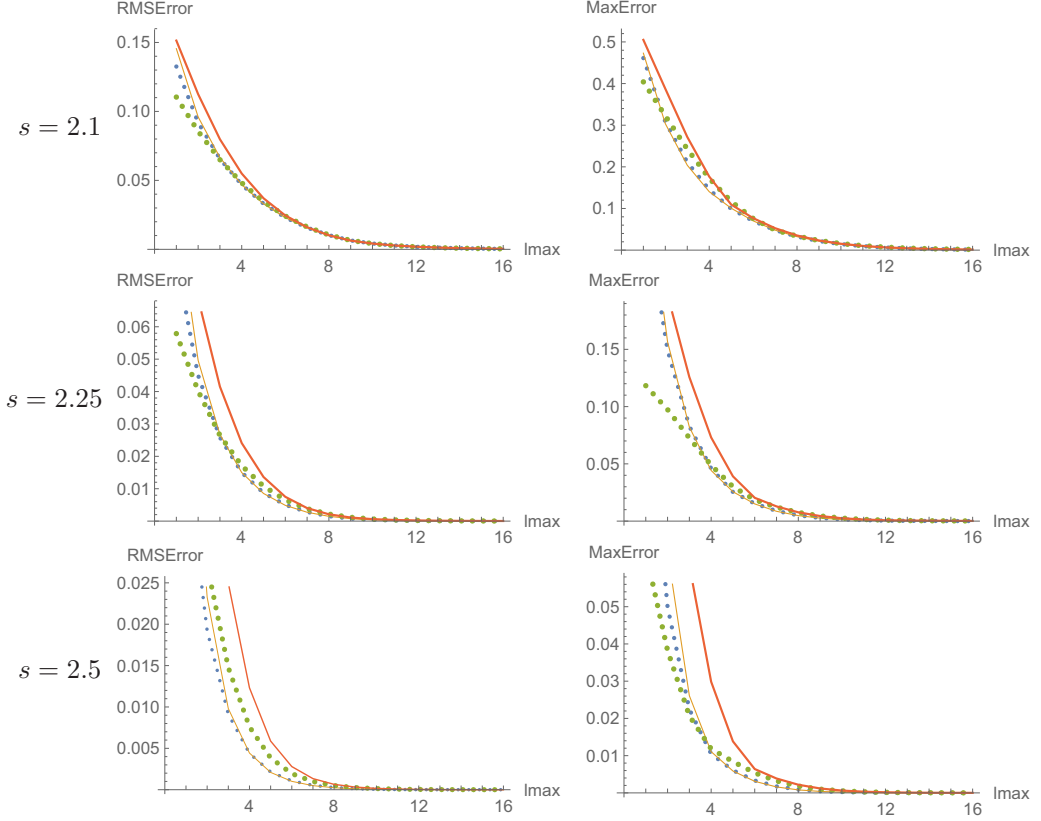


FIG. 3. Spectral convergence for tangential translation along x with RMS error (left panel) and maximum error (right panel) where γ is i (thin dotted line), 1 (thin solid line), $10i$ (thick dotted line), and 10 (thick solid line). The rows represent different separations s as displayed.

relative motion between closely situated surface elements from two spheres along a single direction on the plane. These cases are described by Figs. 3 and 4, respectively. The associated errors in both are of the similar nature, and are consistently less than what we have seen in Fig. 2. The errors decrease below 0.1% even for the tightest configuration, when l_{\max} is 16. The axial symmetry dictates that the plots should be identical between motions along x and y axes. We verified this fact by representative computations.

In Fig. 5, we present spectral convergence for normal rotation of the second sphere along the z axis. Such motion creates relative movement in tangential plane so that most proximate surface elements of two spheres slide without unidirectional preference. In steady Stokesian dynamics, the errors remain least in these situation compared to other cases. In Fig. 5 also, the errors are consistently less than the same in Figs. 2–4.

All curves in Figs. 2–5 exhibit exponential convergence typical in spectral methods based on basis function expansions. Thus, our scheme is especially efficient in simulating even difficult geometries. We performed the simulation in 2.4 GHz laptop using Mathematica codes. The computation time for a single geometry with such a set up is only order of a few seconds, when l_{\max} is considered as 16. This time can be further reduced by more efficient coding in more computing friendly languages. Nevertheless, even with our codes and machines, we can describe many-body Brownian dynamics with time-dependent hydrodynamic interactions.

In all cases, we also located the surface grid at which the error is maximum. As expected, this region of substantial error on both spheres is in vicinity of the point which is nearest to the other

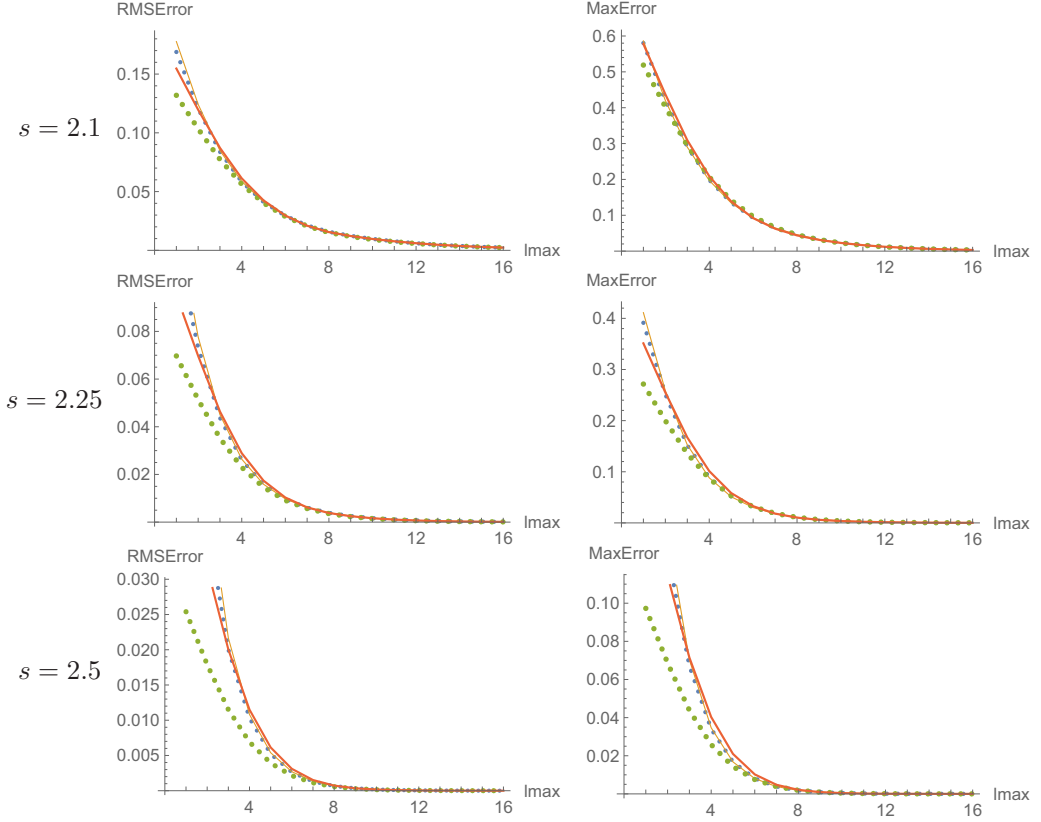


FIG. 4. Spectral convergence for tangential rotation along x with RMS error (left panel) and maximum error (right panel), where γ is i (thin dotted line), 1 (thin solid line), $10i$ (thick dotted line), and 10 (thick solid line). The rows represent different separations s as displayed.

sphere. It is always difficult to construct \mathbf{v} in the domain in between two particles by using spherical basis functions. The position of maximum error is indicative of this fact.

Errors are more or less similar in magnitude for all γ . This shows that wave number does not contribute substantially in computational complexities as long as its inverse remains of the same order of surface-to-surface separation.

C. Spectral convergence results for three-sphere systems

In our next validation test, we consider a system with equally sized spheres (radius $a_1 = a_2 = a_3 = a$) whose centers are located on the z axis. The middle particle is equally separated by a distance s from the two at the extreme. Thus, the geometry has both axial symmetry about z axis and reflectional symmetry about the middle sphere across its diametrical plane perpendicular to the central line. The system is schematically presented in Fig. 1. We choose s as $2.1 * a$ which is the most difficult geometry to simulate among the ones considered in the two-body analysis due to small surface-to-surface separation.

The velocity field is generated by the axial translation of two extreme spheres while the middle one remained fixed. As seen in Sec. III B, such axial motions presents most difficult convergence challenges due to normal relative motion between two separate surfaces at the region of closest proximity. There are two cases considered in the simulation. In the first problem, the translating spheres are moving in the same direction, whereas the second one assumes their opposing motion.

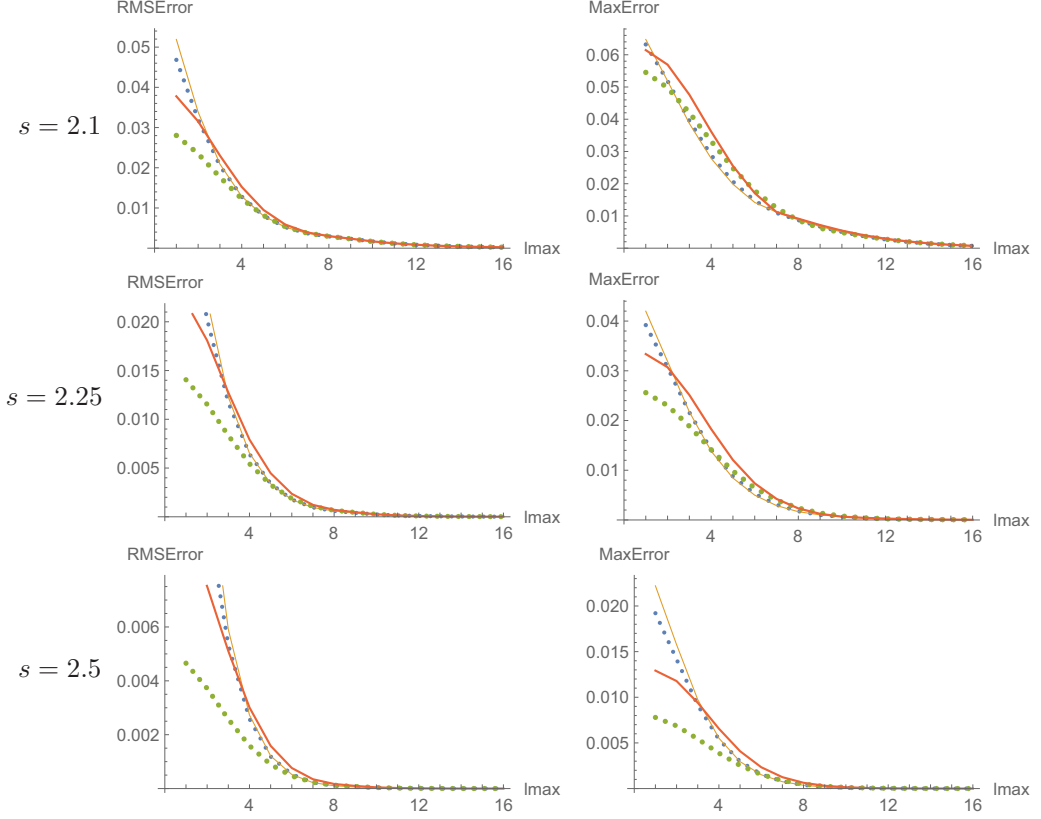


FIG. 5. Spectral convergence for normal rotation along z with RMS error (left panel) and maximum error (right panel), where γ is i (thin dotted line), 1 (thin solid line), $10i$ (thick dotted line), and 10 (thick solid line). The rows represent different separations s as displayed.

We are interested in computing the velocity field at the surface of the static sphere in the middle. If the simulation is accurate with correct transformation coefficients and basis functions, then the velocity at this surface should approach 0 with increasing l_{\max} . Any nonzero interfacial velocity should be viewed as the measure of computational error. This is why we calculate its RMS and maximum value at the grid points on the intermediate spheres like in two-body simulation, and plot these as functions of l_{\max} . Like before in Figs. 2–5, four values of γ are chosen. These spectral convergence plots for both unidirectional and opposing motions of two extreme spheres are presented in Fig. 6.

For large spectral order l_{\max} , the curves in Fig. 6 exhibit similar convergence characteristics as in Fig. 2 with $s = 2.1$. Like before, the relative error seems to be less than 1% when l_{\max} is 16 or more. This proves the applicability of our methodology for systems with large number of spheres.

For smaller l_{\max} , however, curves in Figs. 2 and 6 have a distinct difference. In two-body systems, the error decreases consistently always. In contrast, three-body simulations exhibit “saw tooth”-type convergence with intermittent reversal in trend. Thus, for small values of l_{\max} , increase in spectral order by a value 1 may cause decrease in accuracy. This is a generic trend in spectral schemes in presence of multiple interfaces observed also in the past studies [19,20]. The reason behind such anomalous behavior is cancellations of higher order multipolar contributions from symmetrically situated neighboring bodies. As a result, odd l_{\max} is relatively better for unidirectional motion because even order multipoles from two peripheral spheres tend to nullify each other causing an

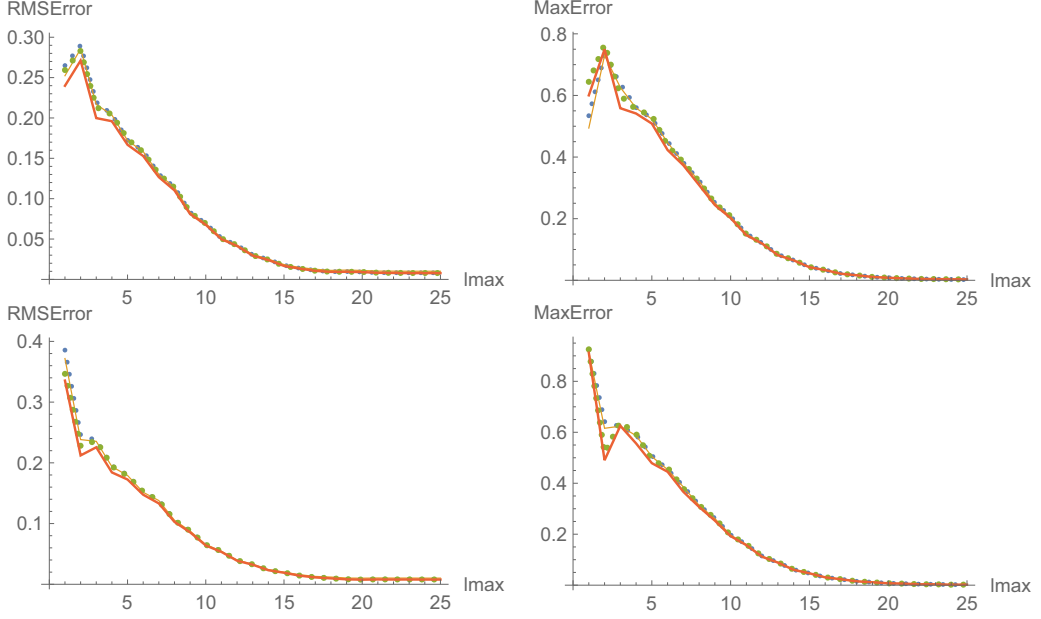


FIG. 6. Spectral convergence for three-sphere system along z with RMS error (left panel) and maximum error (right panel), where γ is i (thin dotted line), 1 (thin solid line), $10i$ (thick dotted line), and 10 (thick solid line). The first row and the second row represent two extreme spheres translating with the same phase and opposite phase, respectively.

unexpected gain in accuracy. In contrast, even order l_{\max} produces a relatively better results for opposing translation, as odd order multipoles from two moving spheres partially cancel effects of each other.

D. Validation with Stokesian results

In the final test, we verify our solution technique for Brinkman equation by calculating two-body friction coefficients and comparing these with their known values. The force and torque on a body due to specified motion of unit magnitude forms the component of friction tensors. Benchmark values of these are readily available in Stokesian dynamics analysis and complementing lubrication theories. However, for $k \rightarrow 0$, quantities derived from Brinkman equation should coincide with Stokesian findings. We exploit this fact to add another additional validation for the developed technique.

We choose a very small value (0.001) for k , and use the outlined scheme to produce the velocity field in a two-sphere system as described in Fig. 1 and in Sec. III B. In the specific problem, one of the sphere is fixed whereas the second one is moving along the line joining two centers with unit speed. The force on moving sphere is referred to as self friction, whereas the one on the static particle due to the induced flow around it is known as mutual coefficient. The symmetry of the geometry dictates that both would be along the same direction of the translational motion.

The values of the self and the mutual frictions are calculated two ways. First, Stokesian algorithm along with lubrication subtractions provides the force on each sphere. Second, the respective surface integrals of hydrodynamic stress corresponding to the velocity and the pressure field for the Brinkman equation solution renders another set of values for the same quantity. This comparison is presented in Table 1 for five different center-to-center distances s .

TABLE I. Normal friction obtained from Stokesian analysis and new solution technique.

	Normal $\mathbf{F}_{tt}^{\text{self}}$		Normal $\mathbf{F}_{tt}^{\text{mutual}}$	
	Stokesian	New scheme $k=0.001$	Stokesian	New scheme $k=0.001$
$s = 2.1$	-76.003	-76.021	63.734	63.716
$s = 2.2$	-49.783	-49.801	37.407	37.389
$s = 2.3$	-40.463	-40.481	27.982	27.964
$s = 2.4$	-35.552	-35.571	22.969	22.950
$s = 2.5$	-32.472	-32.491	19.787	19.768

The first set of data is obtained using converged Stokesian results with accelerated convergence caused by application of higher order lubrication theory. Then, we use $l_{\max}=20$ in the solution technique for Brinkman equation without any theoretically calculated lubrication analysis to create the second set of values. It is evident in Table 1 that the two sets of findings coincide emphatically.

IV. VISUALIZATION OF FLOWS GOVERNED BY BRINKMAN EQUATION

This section demonstrates relevance of our solution scheme for Brinkman equation in a wide range of fluid mechanics problems. The versatility of our scheme is showcased by describing two apparently unrelated flow phenomena. We present the solution of the velocity field obtained by the outlined algorithm in streamline diagrams for both cases.

A. Fluid squeezed by two impermeable spheres in porous medium

In our first simulation, we consider two impermeable spheres inside a porous medium filled with viscous liquid. The porosity of the domain is defined by $\gamma = 1$ representing a relatively relaxed and soft matrix. The spheres are squeezing the fluid slowly by approaching towards each other with a nondimensional speed 0.5. The velocity scale is such that the spheres are displaced very little during the observation timescale so that we can assume a quasisteady hydrodynamic field despite the slow change in geometry.

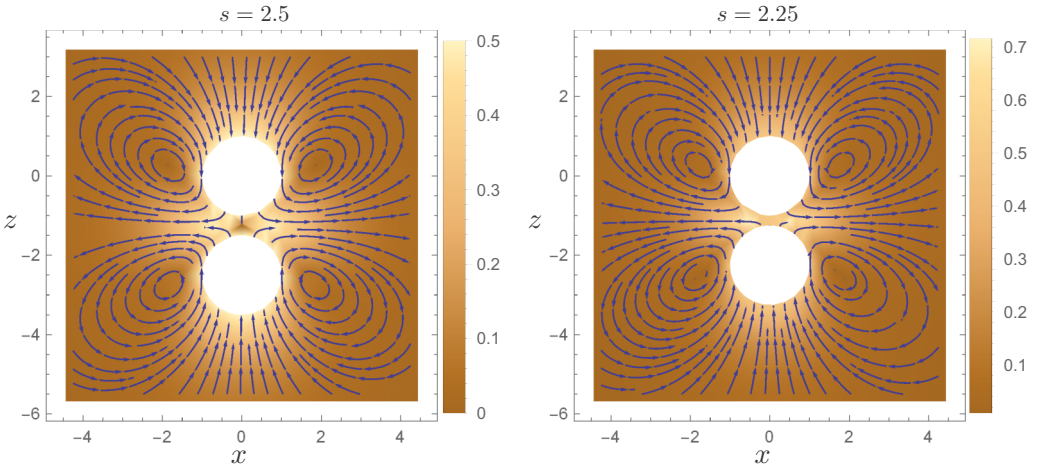


FIG. 7. Streamlines for flow field in a porous medium around two impermeable spheres moving towards each other ($\gamma = 1$) with center-to-center separation $s = 2.5 * a$ and $s = 2.25 * a$.

In Fig. 7, we show the velocity field around the spheres using streamlines with flow-strength shade plots. Two initial separations are chosen to depict the quasisteady flow.

When the particles are relatively more separated, the flow-strength shade plot reveals a maximum velocity of 0.5 which coincides with the speed of the spheres. In contrast, when these are closer to each other, the maximum velocity in the domain increases considerably. This happens because the velocity in the contact region perpendicular to the line joining the centers enhances significantly, as the closely situated solid bodies squeezes the fluid out. The proper depiction of such lubrication flow without any explicit contribution from any asymptotic analysis shows both the accuracy and capacity of the developed algorithm.

In both plots in Fig. 7, one can notice four vortices in four quadrants. The vortices in adjacent quadrants are counter-rotating to each other. Such feature conforms with intuitive understanding of the flow field where the squeezed out fluid has to circulate back by the far-field flow compensating the volume displaced by the translating spheres.

B. Unsteady velocity field created by two oscillating spheres with opposite phase

Our second study focuses on small amplitude oscillation of two closely situated spheres in free viscous fluid. The particles are vibrating along the line joining their centers. Their sinusoidal motions have opposite phase so that they either squeeze or stretch the liquid in between. The period of oscillation matches with viscous timescale making $\gamma = i$ or $k = \sqrt{i}$.

The separation s is the average distance between two centers or the gap at the equilibrium position during the course of the sinusoidal motion. The amplitude of oscillation is considered very small causing subdominant convection as well as negligible change in geometry. Two values of s are chosen to explore the impact of equilibrium distance on flow.

The considered flow phenomenon involves an inherently unsteady velocity field induced by small amplitude but quickly fluctuating translations of the spheres. However, such dependence on time can be represented by two temporally independent fields. The solution of the Brinkman equation with $\gamma = i$ is a time-invariant complex function with both real and imaginary parts. When these functions are coupled with sinusoidal temporal variations, one can generate the desired velocity as function of both space and time.

In Fig. 8, we present both the real and imaginary parts of complex \mathbf{v} for two equilibrium separations by using streamlines and flow-strength shades. The physical interpretation of the real part of \mathbf{v} is the instantaneous velocity field created when both particles are at their equilibrium position with maximum speed during their course of sinusoidal motion. In contrast, the imaginary part represents the fluid motion when both spheres reach their extremum positions. At that point, the two bodies are momentarily static, though the liquid far from these can still moves due to the inertial effect. This manifestation of inertia is a key difference between the systems under current consideration and the Stokesian dynamics.

When oscillating particles are at the equilibrium position with maximum speed, the instantaneous velocity field represented by the real part of \mathbf{v} in Fig. 8 is very similar to the plots in Fig. 7. The vortices as well as more enhanced flow in narrower gap are almost identical, though the actual values in reality varies within 10% between two systems. Such similarities are expected because these are essentially same flows from physical perspective.

In contrast, the flow-structures around the momentarily static spheres at their extreme locations represented by the imaginary part of \mathbf{v} are quite different than the ones seen when the solid bodies are moving. There are mainly three significant differences. First, the purely inertial flow with no active drag by moving particles is weaker in strength as manifested by the color bar for the shade plots. Second, the lubrication region exhibits nearly no flow as the liquid is trapped between two static spheres. Finally, the counter-rotating vortices are further away from the immobile solids, as inertial effect is only prominent away from these.

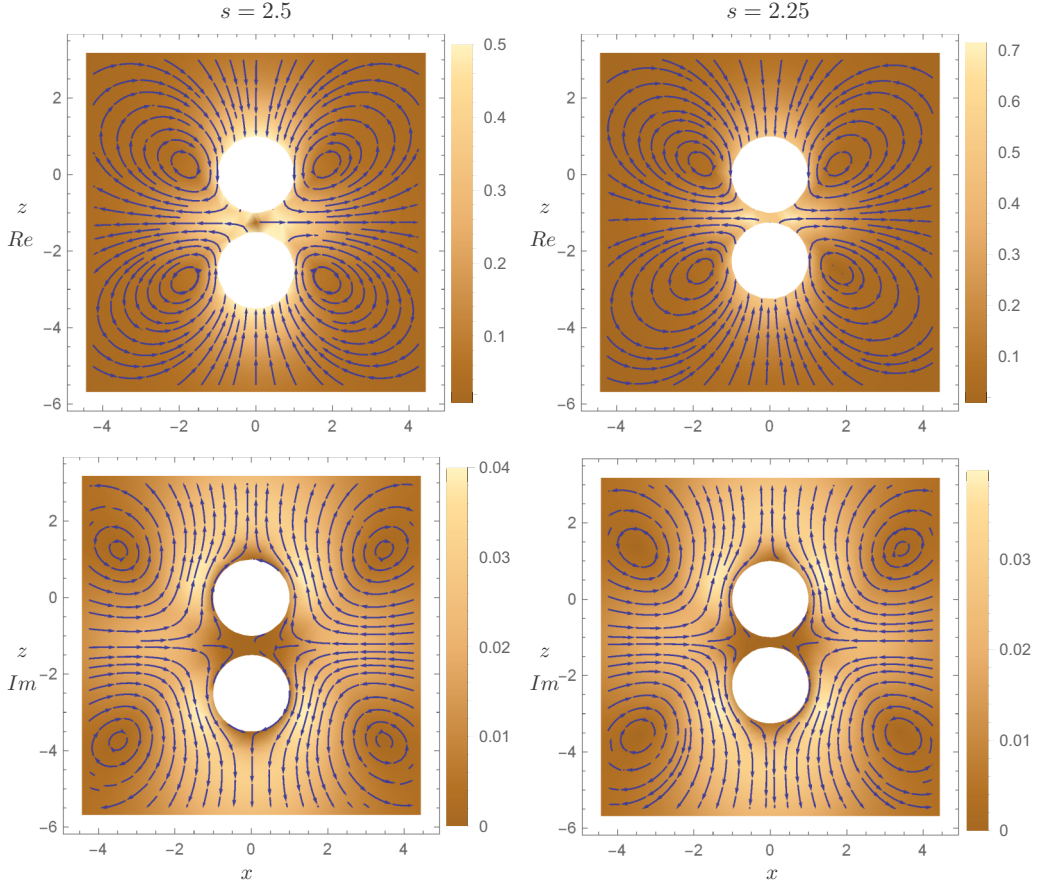


FIG. 8. Streamlines created by two oscillating spheres with opposite phase, where $k = \sqrt{i}$ and center-to-center equilibrium separation $s = 2.5$ (left panel) and $s = 2.25$ (right panel). The first row and the second row correspond to real part and imaginary part of the velocity field which represent the instantaneous flow at equilibrium and the extreme positions of the particles, respectively.

V. SUMMARY AND CONCLUDING REMARKS

This article describes a novel methodology to solve for a vector field governed by Brinkman equation where inhomogeneous boundary conditions are provided at the surface of many spheres in proximity. The wave number associated to the governing equation can be either real or imaginary or complex depending on the specific phenomenon from which it is derived. For example, in a steady flow in heterogeneous porous medium the square of the wave number assumes real values, whereas in unsteady Stokes problem the same remains a purely imaginary quantity. The outlined scheme is valid for all these wide ranging problems.

The method is based on the expansion of the dependent variable, vector \mathbf{v} , in the basis functions of Brinkman equation centered around each particle. This is similar to the many-body simulation involving either steady Stokes flows or potential harmonic fields, though the scope of the outlined scheme is much wider than its predecessors. The most important and nontrivial step in our mathematical formulation is the derivation of the transformation coefficients which relate basis functions around one point in terms of the same around another. This allow us to couple the reflected contribution in \mathbf{v} from one particle to the field induced at the surface of others. Consequently, we

can construct a matrix representation where inhomogeneous boundary conditions on all spheres are simultaneously satisfied.

Our scheme is applied to simulate a two- and three-sphere systems. The main purpose of these computations are to demonstrate the accuracy and the efficiency of the proposed technique. This goal is achieved by the simplest possible way. First, we check whether the computed \mathbf{v} satisfies the governing relation by using finite difference. Then, we quantify how much the constructed \mathbf{v} deviates from the prescribed boundary conditions. The maximum and the RMS values of such interfacial error are plotted with increasing number of considered basis functions to estimate the accuracy and to investigate the convergence rate. Also, the new technique is used to calculate Stokesian friction values under appropriate limits for purpose of comparison.

For different geometries as well as for different wave numbers, the simulation results demonstrate a consistent convergence characteristics of exponential nature. Even if the surface-to-surface separation is one order of magnitude less than the spherical dimensions, a spectral size with maximum value of the harmonic index $l_{\max} = 16$ is enough to ensure less than 1% error. The number of involved basis functions are then such that a simulation can be completed within a second using mathematica. The efficiency of computation makes the formulated method ideal for flow-analysis in larger systems like many-particle transient Brownian medium or multicomponent porous filter.

The geometry plays a crucial role in incurring error or determining computation time. A closely situated pair of spheres is more difficult to simulate, because it is problematic to reproduce \mathbf{v} inside the gap between two particles. In such situation, increased number of basis functions would be needed. In contrast, fields around widely separated spheres can be accounted for much faster with reduced number of basis functions. This contrast opens up further enhancement in efficiency for many-body simulation, where the spectral size in a matrix block is dictated by the mutual separations between particles.

The value or nature of the wave number does not have significant impact on the computational time or numerical accuracy. The errors are more or less similar for both real and complex wave numbers.

The outlined methodology can be a very useful computational tool in simulation of numerous complex systems. This assertion is proven by flow simulations involving two apparently different systems. In the first study, the velocity field is created due to impermeable spheres squeezing liquid in a porous medium. In the second investigation, unsteady transport around two sinusoidally oscillating particle is described. This demonstrates the versatility and potential applicability of our method.

Noticing the unique capability of the developed algorithm, we are planning to use it to quantify the cumulative effect of many Brownian particles on the fluctuating microscale flow dragged by the suspended species. Such phenomenon is akin to a medium where multiple stirrer enhances the heat transfer if a temperature gradient is established. As a result, we will be able to provide a quantitative theory for nanofluidic properties. Similarly, the same multiparticle interactions causes error in microrheological prediction of viscoelastic properties of a solvent, if several tracer Brownian bodies are present in the system. In the near future, we can correct this inaccuracy by estimating the transient effect of one particle on another.

The data that support the findings of this study are available from the corresponding author upon reasonable request.

ACKNOWLEDGMENT

This work is supported by NSF Grant No. CBET-1805930.

APPENDIX: DERIVATION OF TRANSFORMATION COEFFICIENTS

This Appendix derives the transformation coefficients $M_{lms\lambda,\mu s'}^{ij\mp}$ coupling singular and regular solutions as the elements of $[M_{12}^{\mp}]$ defined in Eq. (20). The derivation, however, depends on $M_{lms\lambda,\mu s'}^{ij=}$

which relate two sets of singular solutions. Accordingly, we arrange $M_{lms\lambda,\mu s'}^{ij=}$ in the matrix $[M_{12}^{\pm}]$ as its elements, and construct it first. Then, the expressions in Sec. II C for $M_{lms\lambda,\mu s'}^{ij\mp}$ or $[M_{12}^{\mp}]$ are subsequently obtained as the final results.

1. Transformation Matrix between singular solutions

To derive $[M_{12}^{\pm}]$, we consider a few crucial identities which are outlined below. These can be easily proved from the properties of the associated Legendre polynomial involved in the spherical harmonics appearing as a separable factor in the basis functions.

The first identity is

$$\frac{\partial \psi_{lm}^{\text{h}\pm}(\mathbf{r}_i)}{\partial z} = \left(\frac{l-m+1}{2l+1} \right) \psi_{(l+1)m}^{\text{h}\pm}(\mathbf{r}_i) + \left(\frac{l+m}{2l+1} \right) k^2 \psi_{(l-1)m}^{\text{h}\pm}(\mathbf{r}_i), \quad (\text{A1})$$

where $\mathbf{r}_i = \mathbf{r} - \mathbf{x}_i$ is the relative position vector of an observation point with respect to the center of the i th sphere situated at $\mathbf{r} = \mathbf{x}_i$. The matrix relation below represents Eq. (A1):

$$\frac{\partial}{\partial z} |\psi_m^{\text{h}\pm}(\mathbf{r}_i)\rangle = [T_m] |\psi_m^{\text{h}\pm}(\mathbf{r}_i)\rangle, \quad (\text{A2})$$

where the column $|\psi_m^{\text{h}\pm}(\mathbf{r}_i)\rangle = \{\psi_{|m|m}^{\text{h}\pm}(\mathbf{r}_i), \psi_{(|m|+1)m}^{\text{h}\pm}(\mathbf{r}_i), \dots, \psi_{lm}^{\text{h}\pm}(\mathbf{r}_i)\}^T$ lists functions $\psi_{lm}^{\text{h}\pm}$ with varying l as elements for specific m . Sparse and bidiagonal $[T_m]$ contains elements $T_{l\lambda}^m$:

$$T_{l\lambda}^m = \frac{(l-m+1)}{(2l+1)} \delta_{(l+1)\lambda} + \frac{(l+m)k^2}{(2l+1)} \delta_{(l-1)\lambda}. \quad (\text{A3})$$

Equation (A3) is what we first introduced in Eq. (26).

Similarly, the second identity is

$$\frac{\partial \psi_{lm}^{\text{PI-}}(\mathbf{r}_i)}{\partial z} = -(l-m+1) \psi_{(l+1)m}^{\text{PI-}}(\mathbf{r}_i). \quad (\text{A4})$$

Also, we convert this relation to a matrix expression,

$$\frac{\partial}{\partial z} |\psi_m^{\text{PI-}}(\mathbf{r}_i)\rangle = [Q_m^-] |\psi_m^{\text{PI-}}(\mathbf{r}_i)\rangle. \quad (\text{A5})$$

Here, $[Q_m^-]$ is a sparse matrix whose elements are

$$Q_{l\lambda}^{m-} = -(l-m+1) \delta_{(l+1)\lambda}, \quad (\text{A6})$$

coinciding with Eq. (A6), and the column $|\psi_m^{\text{PI-}}(\mathbf{r}_i)\rangle$ is $\{\psi_{|m|m}^{\text{PI-}}(\mathbf{r}_i), \psi_{(|m|+1)m}^{\text{PI-}}(\mathbf{r}_i), \dots, \psi_{lm}^{\text{PI-}}(\mathbf{r}_i)\}^T$.

The third and fourth identities below complete the required relations for our derivations:

$$\mathbf{v}_{lm1}^{i\pm} = -k^2 \nabla \times \mathbf{v}_{lm2}^{i\pm}, \quad (\text{A7})$$

and

$$\hat{\mathbf{e}}_z \times \nabla \psi_{lm}^{\text{h}\pm}(\mathbf{r}_i) = \frac{im}{l(l+1)} \mathbf{v}_{lm2}^{i\pm} - \frac{(l-m+1)}{(2l+1)(l+1)} \mathbf{v}_{(l+1)m1}^{i\pm} + \frac{(l+m)}{(2l+1)l} k^2 \mathbf{v}_{(l-1)m1}^{i\pm}. \quad (\text{A8})$$

The last identity corresponds to the following matrix relation:

$$\hat{\mathbf{e}}_z \times \nabla |\psi_m^{\text{h}\pm}(\mathbf{r}_i)\rangle = [R_m] |\mathbf{v}_{m1}^{i\pm}\rangle + [C_m] |\mathbf{v}_{m2}^{i\pm}\rangle. \quad (\text{A9})$$

Here, $|\mathbf{v}_{ms}^{i\pm}\rangle$ has similar form like $|\psi_m^{\text{h}\pm}(\mathbf{r}_i)\rangle$, so that $|\mathbf{v}_{ms}^{i\pm}\rangle = \{\mathbf{v}_{|m|ms}^{i\pm}, \mathbf{v}_{(|m|+1)ms}^{i\pm}, \dots, \mathbf{v}_{lms}^{i\pm}\}^T$. The sparse diagonal matrix $[R_m]$ and diagonal matrix $[C_m]$ have elements as

$$R_{l\lambda}^m = -\frac{(l-m+1)}{(2l+1)(l+1)} \delta_{(l+1)\lambda} + \frac{(l+m)k^2}{(2l+1)l} \delta_{(l-1)\lambda}, \quad (\text{A10})$$

and

$$C_{l\lambda}^m = \frac{im}{l(l+1)} \delta_{l\lambda}. \quad (\text{A11})$$

These are mentioned in Eqs. (23) and (24) in the earlier narration, respectively.

After all the necessary identities are identified, transformation matrix $[M_{12}^-]$ can be derived in the following way. For the region $|\mathbf{r}_2| > |s|$, we are allowed to expand column $|\psi_m^{\text{h-}}(\mathbf{r}_2 + s\hat{\mathbf{e}}_z)\rangle$ in Taylor series. Also, from Eqs. (A2) and (A9), we find that

$$\begin{aligned} |\mathbf{v}_{m1}^{1-}\rangle &= \mathbf{r}_1 \times \nabla |\psi_m^{\text{h-}}(\mathbf{r}_1)\rangle = (\mathbf{r}_2 + s\hat{\mathbf{e}}_z) \times \nabla |\psi_m^{\text{h-}}(\mathbf{r}_2 + s\hat{\mathbf{e}}_z)\rangle \\ &= (\mathbf{r}_2 + s\hat{\mathbf{e}}_z) \times \nabla \left(|\psi_m^{\text{h-}}(\mathbf{r}_2)\rangle + s \left| \frac{\partial \psi_m^{\text{h-}}(\mathbf{r}_2)}{\partial z} \right\rangle + \cdots + \frac{s^n}{n!} \left| \frac{\partial^n \psi_m^{\text{h-}}(\mathbf{r}_2)}{\partial z^n} \right\rangle \right) \\ &= \mathbf{r}_2 \times \nabla ([T'_m] |\psi_m^{\text{h-}}(\mathbf{r}_2)\rangle) + s\hat{\mathbf{e}}_z \times \nabla ([T'_m] |\psi_m^{\text{h-}}(\mathbf{r}_2)\rangle) \\ &= [T'_m] |\mathbf{v}_{m1}^{2-}\rangle + s[T'_m][R_m] |\mathbf{v}_{m1}^{2-}\rangle + s[T'_m][C_m] |\mathbf{v}_{m2}^{2-}\rangle. \end{aligned} \quad (\text{A12})$$

Here, matrix $[T'_m]$ is constructed in the following relation:

$$[T'_m] = \sum_{n=0}^{n_{\max}} \frac{s^n}{n!} [T_m]^n, \quad (\text{A13})$$

where the upper limit n_{\max} has to be considerably greater than $e * s * |k|/\sqrt{2}$ for good convergence. The relation Eq. (A13) is first displayed in the main text as Eq. (28). In the next step, we take curl of Eq. (A12) and use Eq. (A7) to derive

$$|\mathbf{v}_{m1}^{1-}\rangle = [T'_m] |\mathbf{v}_{m2}^{2-}\rangle + s[T'_m][R_m] |\mathbf{v}_{m2}^{2-}\rangle - k^2 s[T'_m][C_m] |\mathbf{v}_{m1}^{2-}\rangle. \quad (\text{A14})$$

Thus, the homogeneous basis solutions of Brinkman equation centered around two different spheres are coupled by Eqs. (A12) and (A14).

We also find the relations between two sets of particular integrals for Brinkman equation constructed as the gradient of the scalar field $|\psi_m^{\text{PI-}}|$. To this end, for $|\mathbf{r}_2| > |s|$, we expand column $|\psi_m^{\text{PI-}}(\mathbf{r}_2 + s\hat{\mathbf{e}}_z)\rangle$ in a Taylor series, and use Eq. (A5) to derive the following:

$$\begin{aligned} |\mathbf{v}_{m3}^{1-}\rangle &= \nabla |\psi_m^{\text{PI-}}(\mathbf{r}_2 + s\hat{\mathbf{e}}_z)\rangle = \nabla \left(|\psi_m^{\text{PI-}}(\mathbf{r}_2)\rangle + s \left| \frac{\partial \psi_m^{\text{PI-}}(\mathbf{r}_2)}{\partial z} \right\rangle + \cdots + \frac{s^n}{n!} \left| \frac{\partial^n \psi_m^{\text{PI-}}(\mathbf{r}_2)}{\partial z^n} \right\rangle \right) \\ &= \nabla \left(|\psi_m^{\text{PI-}}(\mathbf{r}_2)\rangle + s[Q_m^-] |\psi_m^{\text{PI-}}(\mathbf{r}_2)\rangle + \cdots + \frac{s^n}{n!} [Q_m^-]^n |\psi_m^{\text{PI-}}(\mathbf{r}_2)\rangle \right) \\ &= \nabla ([Q_m^{-'}] |\psi_m^{\text{PI-}}(\mathbf{r}_2)\rangle) = [Q_m^{-'}] |\mathbf{v}_{m3}^{2-}\rangle. \end{aligned} \quad (\text{A15})$$

Here, $[Q_m^{-'}]$ becomes a diagonal dominant, but nonsparse matrix, where

$$[Q_m^{-'}] = \sum_{n=0}^{n_{\max}} s^n [Q_m^-]^n / n!. \quad (\text{A16})$$

We have introduced Eq. (A16) in Eq. (31) of the main text also.

Finally, we use a matrix expression to combine Eqs. (A12), (A14), and (A15) concluding

$$[M_m^{12=}] = \begin{bmatrix} [T'_m] + s[T'_m][R_m] & s[T'_m][C_m] & 0 \\ -k^2 s[T'_m][C_m] & [T'_m] + s[T'_m][R_m] & 0 \\ 0 & 0 & [Q_m^{-'}] \end{bmatrix}. \quad (\text{A17})$$

Here, matrix $[M_m^{12=}]$ is the block in transformation matrix $[M_{12}^-]$ for a specific m . So matrix $[M_{12}^-]$ can be derived by combining submatrices $[M_m^{12=}]$ for all different values of m .

2. Transformation matrix between singular solution and regular solution

Next, $[M_{12}^{\mp}]$ is constructed from $[M_{12}^{\pm}]$. Complexity of a general submatirx $[M_m^{12=}]$ for any arbitrary m will obscure the key results. Instead, we only take into account matrix $[M_m^{12\mp}]$ for $m = 0, \pm 1$ and consider them separately, as these are only relevant m 's for our systems. The derivation requires a few additional identities involving the basis solutions of Brinkman equation. These relations are classified into two groups.

First, we need an identity analogous to Eq. (A4) with only $\psi_{lm}^{\text{PI}+}$ replacing $\psi_{lm}^{\text{PI}-}$:

$$\frac{\partial \psi_{lm}^{\text{PI}+}(\mathbf{r}_i)}{\partial z} = (l+m)\psi_{(l-1)m}^{\text{PI}+}(\mathbf{r}_i). \quad (\text{A18})$$

The corresponding matrix representation for this identity is

$$\frac{\partial}{\partial z} |\psi_m^{\text{PI}+}(\mathbf{r}_i)\rangle = [Q_m^+] |\psi_m^{\text{PI}+}(\mathbf{r}_i)\rangle. \quad (\text{A19})$$

Here, $[Q_m^+]$ is a lower-diagonal matrix whose elements are

$$Q_{l\lambda}^{m+} = (l+m)\delta_{(l-1)\lambda}, \quad (\text{A20})$$

which is also displayed in Eq. (30).

The second group of identities helps us to derive results for different values of m from the ones associated to $m=0$. These use raising and lowering operators in quantum mechanics, where m is increased or decreased by the operation. Our two sphere system specifically uses two such identities. The first includes the scalar potential for the homogeneous solution:

$$\left(\frac{\partial}{\partial x} + i\frac{\partial}{\partial y}\right) |\psi_0^{\text{h}\pm}(\mathbf{r}_i)\rangle = [A^{\text{h}}] |\psi_1^{\text{h}\pm}(\mathbf{r}_i)\rangle, \quad \text{and} \quad \left(\frac{\partial}{\partial x} - i\frac{\partial}{\partial y}\right) |\psi_0^{\text{h}\pm}(\mathbf{r}_i)\rangle = [B^{\text{h}}] |\psi_{(-1)}^{\text{h}\pm}(\mathbf{r}_i)\rangle. \quad (\text{A21})$$

Here submatrix $[A^{\text{h}}]$ and $[B^{\text{h}}]$ are bidiagonal with elements $A_{l\lambda}^{\text{h}}$ and $B_{l\lambda}^{\text{h}}$, respectively:

$$A_{l\lambda}^{\text{h}} = \left(\frac{-1}{2l+1}\right)\delta_{l\lambda} + \left(\frac{k^2}{2l+1}\right)\delta_{(l-2)\lambda}, \quad B_{l\lambda}^{\text{h}} = \frac{(l+1)(l+2)}{(2l+1)}\delta_{l\lambda} - \frac{l(l-1)k^2}{(2l+1)}\delta_{(l-2)\lambda}. \quad (\text{A22})$$

These are what we first introduced in Eqs. (33) and (35), respectively. Similarly raising and lowering operators can act on the scalar potential for the particular integral so that

$$\left(\frac{\partial}{\partial x} + i\frac{\partial}{\partial y}\right) |\psi_0^{\text{PI}\pm}\rangle = [A^{\text{PI}\pm}] |\psi_1^{\text{PI}\pm}\rangle \quad \text{and} \quad \left(\frac{\partial}{\partial x} - i\frac{\partial}{\partial y}\right) |\psi_0^{\text{PI}\pm}\rangle = [B^{\text{PI}\pm}] |\psi_{(-1)}^{\text{PI}\pm}\rangle. \quad (\text{A23})$$

The elements of the submatrices $[A^{\text{PI}+}]$, $[A^{\text{PI}-}]$, $[B^{\text{PI}+}]$, $[B^{\text{PI}-}]$ are as below

$$A_{l\lambda}^{\text{PI}+} = \delta_{(l-2)\lambda}, \quad A_{l\lambda}^{\text{PI}-} = \delta_{l\lambda}, \quad B_{l\lambda}^{\text{PI}+} = -l(l-1)\delta_{(l-2)\lambda}, \quad B_{l\lambda}^{\text{PI}-} = -(l+1)(l+2)\delta_{l\lambda}. \quad (\text{A24})$$

Noting $[A^{\text{PI}-}]$ is simply the identity matrix, $[A^{\text{PI}+}]$ is referred as $[A^{\text{PI}}]$ in the main article. The remaining components in Eq. (A24) are also furnished there as Eqs. (36) and (37).

The aforementioned identities are first utilized in derivation of $[M_m^{12\mp}]$ for $m = 0$. For this purpose, we conclude from Eqs. (A2) and (A13) that Taylor series expansion yields

$$|\psi_0^{\text{h}-}(\mathbf{r}_1)\rangle = [T_0'] |\psi_0^{\text{h}-}(\mathbf{r}_2)\rangle, \quad (\text{A25})$$

when $|\mathbf{r}_2| > |s|$. With a similar rationale, we argue that when $|\mathbf{r}_2| < |s|$,

$$|\psi_0^{\text{h}-}(\mathbf{r}_1)\rangle = [\bar{T}_0'] |\psi_0^{\text{h}+}(\mathbf{r}_2)\rangle, \quad (\text{A26})$$

where $[\bar{T}_0']$ is a transformation matrix we need to derive later. Since $\psi_{00}^{\text{h}\pm}(\mathbf{r}_i)$ are isotropic functions without any angular variation, Eqs. (A25) and (A26) should converge to the same value when $l = 0$, $m = 0$, $|\mathbf{r}_2| \rightarrow |s|$. This statement is represented by

$$\langle e_1 | [T_0'] | \psi_0^{\text{h}-}(s) \rangle = \langle e_1 | [\bar{T}_0'] | \psi_0^{\text{h}+}(s) \rangle, \quad (\text{A27})$$

where the first element of the row $\langle e_1 | = \langle 1, 0, \dots, 0 |$ is 1 and others are 0. Also, when $|\mathbf{r}_2| = s$,

$$|\psi_0^{h-}(s)\rangle = [D_h]|\psi_0^{h+}(s)\rangle. \quad (\text{A28})$$

The elements of diagonal $[D_h]$ are

$$D_{l\lambda}^h = \{g_l^-(s)/g_l^+(s)\}\delta_{l\lambda}, \quad (\text{A29})$$

first introduced in Eq. (27).

Combining Eqs. (A27) and (A28) we find

$$\langle e_1 | [T'_0] [D_h] | \psi_0^{h+}(s) \rangle = \langle e_1 | [\bar{T}_0] | \psi_0^{h+}(s) \rangle \Rightarrow \langle e_1 | [T'_0] [D_h] = \langle e_1 | [\bar{T}_0] \quad (\text{A30})$$

to be self evident. Replacing the conclusion of Eq. (A30) in Eq. (A26), one infers

$$\langle e_1 | \psi_{l0}^{h-}(\mathbf{r}_1) \rangle = \langle e_1 | [T'_0] [D_h] | \psi_{l0}^{h+}(\mathbf{r}_2) \rangle, \quad (\text{A31})$$

when $|\mathbf{r}_2| < |s|$. Then, if we take the derivative $\frac{\partial}{\partial z}$ on both sides of Eq. (A31), Eq. (A2) ensures

$$\langle e_1 | [T_0] | \psi_{l0}^{h-}(\mathbf{r}_1) \rangle = \langle e_1 | [T'_0] [D_h] [T_0] | \psi_{l0}^{h+}(\mathbf{r}_2) \rangle. \quad (\text{A32})$$

Similarly, successive higher-order derivatives $\frac{\partial^l}{\partial z^l}$ on both sides of Eq. (A31) provide a series of equations similar to Eq. (A32). The matrix representation of these relations would be

$$[N_1^h] | \psi_0^{h-}(\mathbf{r}_1) \rangle = [N_2^h] | \psi_0^{h+}(\mathbf{r}_2) \rangle \Rightarrow | \psi_0^{h-}(\mathbf{r}_1) \rangle = [N_1^h]^{-1} [N_2^h] | \psi_0^{h+}(\mathbf{r}_2) \rangle,$$

$$\text{where } [N_1^h] = \begin{bmatrix} \langle e_1 | [I] \\ \langle e_1 | [T_0] \\ \langle e_1 | [T_0]^2 \\ \vdots \\ \langle e_1 | [T_0]^l \end{bmatrix}, \quad [N_2^h] = \begin{bmatrix} \langle e_1 | [T'_0] [D_h] \\ \langle e_1 | [T'_0] [D_h] [T_0] \\ \langle e_1 | [T'_0] [D_h] [T_0]^2 \\ \vdots \\ \langle e_1 | [T'_0] [D_h] [T_0]^l \end{bmatrix}, \quad (\text{A33})$$

as long as $|\mathbf{r}_2| < |s|$. The relations in Eq. (A33) is also narrated in Eq. (25).

Finally, we combine Eqs. (A12) and (A33) to derive

$$|\mathbf{v}_{m1}^{1-}\rangle = [N_1^h]^{-1} [N_2^h] |\mathbf{v}_{m1}^{2+}\rangle + s [N_1^h]^{-1} [N_2^h] [R_m] |\mathbf{v}_{m1}^{2+}\rangle \quad \text{for } |\mathbf{r}_2| < |s|, \quad m = 0. \quad (\text{A34})$$

Also from the definition of basis solutions in Eq. (4), one finds

$$|\mathbf{v}_{m2}^{1-}\rangle = [N_1^h]^{-1} [N_2^h] |\mathbf{v}_{m2}^{2+}\rangle + s [N_1^h]^{-1} [N_2^h] [R_m] |\mathbf{v}_{m2}^{2+}\rangle \quad \text{for } |\mathbf{r}_2| < |s|, \quad m = 0. \quad (\text{A35})$$

These render parts of the transformation relation involving the homogeneous solutions of regular and singular types for Brinkman equation, when $m=0$.

A similar strategy can also be applied to obtain the relation between particular integrals $|\mathbf{v}_{m3}^{1-}\rangle$ and $|\mathbf{v}_{m3}^{2+}\rangle$. Accordingly, Eqs. (A9) and (A16) imply a Taylor series when $|\mathbf{r}_2| > |s|$:

$$|\psi_0^{\text{PI-}}(\mathbf{r}_1)\rangle = [Q_0^{-'}] |\psi_0^{\text{PI-}}(\mathbf{r}_2)\rangle. \quad (\text{A36})$$

Also, when $|\mathbf{r}_2| < |s|$, we assume

$$|\psi_0^{\text{PI-}}(\mathbf{r}_1)\rangle = [Q_0^{-'}] |\psi_0^{\text{PI+}}(\mathbf{r}_2)\rangle, \quad (\text{A37})$$

where $[Q_0^{-'}]$ is to be constructed.

As $\psi_{00}^{\text{PI}\pm}(\mathbf{r}_i)$ are also isotropic functions like $\psi_{00}^{h\pm}(\mathbf{r}_i)$, Eqs. (A36) and (A37) should converge to the same value when $l=0$, $m=0$, $|\mathbf{r}_2| \rightarrow |s|$. This infers

$$\langle e_1 | [Q_0^{-'}] | \psi_0^{\text{PI-}}(s) \rangle = \langle e_1 | [\bar{Q}_0^{-'}] | \psi_0^{\text{PI+}}(s) \rangle. \quad (\text{A38})$$

When $|\mathbf{r}_2| = |s|$, we also have

$$|\psi_0^{\text{PI-}}(s)\rangle = [D_{\text{PI}}] |\psi_0^{\text{PI+}}(s)\rangle, \quad (\text{A39})$$

where elements $D_{l\lambda}^{\text{PI}} = |s|^{-2l-1} \delta_{l\lambda}$ of diagonal $[D_{\text{PI}}]$ are first introduced in Eq. (30). From Eqs. (A38) and (A39), we conclude $\langle e_1 | [Q_0^{-}] | [D_{\text{PI}}] \rangle = \langle e_1 | [Q_0^{-}] \rangle$ which is analogous to Eq. (A30) for homogeneous solutions. Combining this with Eq. (A37), we derive the following when $|\mathbf{r}_2| < |s|$:

$$\langle e_1 | \psi_0^{\text{PI}-}(\mathbf{r}_1) \rangle = \langle e_1 | [Q_0^{-}] | [D_{\text{PI}}] | \psi_0^{\text{PI}+}(\mathbf{r}_2) \rangle. \quad (\text{A40})$$

Next, taking the derivative $\frac{\partial}{\partial z}$ on both sides of Eq. (A40) yields

$$\langle e_1 | [Q_0^{-}] | \psi_0^{\text{PI}-}(\mathbf{r}_1) \rangle = \langle e_1 | [Q_0^{-}] | [D_{\text{PI}}] | [Q_0^{+}] | \psi_0^{\text{PI}+}(\mathbf{r}_2) \rangle. \quad (\text{A41})$$

Similarly, higher-order derivatives $\frac{\partial^l}{\partial z^l}$ of Eq. (A40) provide matrix equation like Eq. (A41),

$$[N_1^{\text{PI}}] | \psi_0^{\text{PI}-}(\mathbf{r}_1) \rangle = [N_2^{\text{PI}}] | \psi_0^{\text{PI}+}(\mathbf{r}_2) \rangle \Rightarrow | \psi_0^{\text{PI}-}(\mathbf{r}_1) \rangle = [N_1^{\text{PI}}]^{-1} [N_2^{\text{PI}}] | \psi_0^{\text{PI}+}(\mathbf{r}_2) \rangle,$$

$$\text{where } [N_1^{\text{PI}}] = \begin{bmatrix} \langle e_1 | [I] \rangle \\ \langle e_1 | [Q_0^{-}] \rangle \\ \langle e_1 | [Q_0^{-}]^2 \rangle \\ \vdots \\ \langle e_1 | [Q_0^{-}]^l \rangle \end{bmatrix}, \quad [N_2^{\text{PI}}] = \begin{bmatrix} \langle e_1 | [Q_0^{-}] | [D_{\text{PI}}] \rangle \\ \langle e_1 | [Q_0^{-}] | [D_{\text{PI}}] | [Q_0^{+}] \rangle \\ \langle e_1 | [Q_0^{-}] | [D_{\text{PI}}] | [Q_0^{+}]^2 \rangle \\ \vdots \\ \langle e_1 | [Q_0^{-}] | [D_{\text{PI}}] | [Q_0^{+}]^l \rangle \end{bmatrix}. \quad (\text{A42})$$

Then, combining Eqs. (4) and (A42), one can conclude

$$| \mathbf{v}_{m3}^{1-} \rangle = [N_1^{\text{PI}}]^{-1} [N_2^{\text{PI}}] | \mathbf{v}_{m3}^{2+} \rangle \quad \text{for } |\mathbf{r}_2| < |s|, \quad m = 0. \quad (\text{A43})$$

This reproduces the earlier results involving harmonic functions given by Ref. [34].

In the end, Eqs. (A34), (A35), and (A43) are combined to derive

$$[M_0^{12\mp}] = \begin{bmatrix} [H_0] + s[H_0][R_0] & 0 & 0 \\ 0 & [H_0] + s[H_0][R_0] & 0 \\ 0 & 0 & [P_0] \end{bmatrix}. \quad (\text{A44})$$

Here, $[H_0] = [N_1^{\text{h}}]^{-1} [N_2^{\text{h}}]$ and $[P_0] = [N_1^{\text{PI}}]^{-1} [N_2^{\text{PI}}]$, while submatrix $[R_0]$ is defined in Eq. (A10). The expression for matrix $[M_0^{12\mp}]$ in Eq. (A44) exactly corresponds to Eq. (22) for $m = 0$.

The subsequent analysis would focus on finding $[M_1^{12\mp}]$ first and $[M_{-1}^{12\mp}]$ next. The expression of $[M_0^{12\mp}]$ with $m=0$ can be used to construct the similar transformation with $m = \pm 1$. For this purpose, we utilize the raising and lowering operators discussed earlier. The mathematical procedure closely follows the technique used in quantum mechanics commonly involving the aforementioned operators.

We take derivative $(\partial/\partial x + i\partial/\partial y)$ on both sides of Eq. (A33) and use Eq. (A21) to find

$$| \psi_1^{\text{h}-}(\mathbf{r}_1) \rangle = [H_1] | \psi_1^{\text{h}+}(\mathbf{r}_2) \rangle. \quad (\text{A45})$$

Here, $[H_1] = [A^{\text{h}}]^{-1} [N_1^{\text{h}}]^{-1} [N_2^{\text{h}}] [A^{\text{h}}]$ is first mentioned in Eq. (32). Then, Eqs. (A12) and (A45) are combined to infer

$$| \mathbf{v}_{m1}^{1-} \rangle = [H_1] | \mathbf{v}_{m1}^{2+} \rangle + s[H_1][R_m] | \mathbf{v}_{m1}^{2+} \rangle + s[H_1][C_m] | \mathbf{v}_{m2}^{2+} \rangle \quad \text{for } |\mathbf{r}_2| < |s|, \quad m = 1. \quad (\text{A46})$$

Also, we conclude from the definition of basis solutions in Eq. (4) that

$$| \mathbf{v}_{m2}^{1-} \rangle = [H_1] | \mathbf{v}_{m2}^{2+} \rangle + s[H_1][R_m] | \mathbf{v}_{m2}^{2+} \rangle - k^2 s[H_1][C_m] | \mathbf{v}_{m1}^{2+} \rangle \quad \text{for } |\mathbf{r}_2| < |s|, \quad m = 1. \quad (\text{A47})$$

Similarly, Eq. (A23) implies

$$| \psi_1^{\text{PI}-}(\mathbf{r}_1) \rangle = [N_1^{\text{PI}}]^{-1} [N_2^{\text{PI}}] [A^{\text{PI}}] | \psi_1^{\text{PI}+}(\mathbf{r}_2) \rangle, \quad (\text{A48})$$

if the same derivative $(\partial/\partial x + i\partial/\partial y)$ is operated on both sides of Eq. (A42) as a raising operator. Consequently, for $|\mathbf{r}_2| < |s|$ and $m = 1$, Eq. (4) allows one to convert Eq. (A48) to the following

relation:

$$|\mathbf{v}_{m3}^{1-}\rangle = [P_1]|\mathbf{v}_{m3}^{2+}\rangle, \quad (\text{A49})$$

assuming a matrix $[P_1]$ defined as $[P_1] = [N_1^{PI}]^{-1}[N_2^{PI}][A^{PI}]$ which is also stated in Eq. (32). Finally, we combine Eqs. (A46), (A47), and (A49) to conclude

$$[M_1^{12\mp}] = \begin{bmatrix} [H_1] + s[H_1][R_1] & s[H_1][C_1] & 0 \\ -k^2s[H_1][C_1] & [H_1] + s[H_1][R_1] & 0 \\ 0 & 0 & [P_1] \end{bmatrix}, \quad (\text{A50})$$

where matrix $[M_1^{12\mp}]$ represents the Eq. (15) for $|\mathbf{r}_2| < |s|$, $m = m' = 1$. Here, matrix $[M_1^{12\mp}]$ is the same matrix first introduced in Eq. (22) for $m = 1$. Submatrices $[R_1]$ and $[C_1]$ are defined in Eqs. (A10) and (A11) for $m = 1$, respectively.

For transformation matrix $[M_m^{12\mp}]$ corresponding to $m = -1$, we could apply the same method as the one we followed in derivation of $[M_1^{12\mp}]$. According to Eq. (A21), the derivative $(\frac{\partial}{\partial x} - i\frac{\partial}{\partial y})$ on both sides of Eq. (A33) yields

$$|\psi_{(-1)}^{\text{h-}}(\mathbf{r}_1)\rangle = [H_{-1}]|\psi_{(-1)}^{\text{h+}}(\mathbf{r}_2)\rangle. \quad (\text{A51})$$

Here, matrix $[H_{-1}] = [B^{\text{h}}]^{-1}[N_1^{\text{h}}]^{-1}[N_2^{\text{h}}][B^{\text{h}}]$, which is first mentioned in Eq. (34). Then combining Eqs. (A12) and (A51), one finds

$$|\mathbf{v}_{m1}^{1-}\rangle = [H_{-1}]|\mathbf{v}_{m1}^{2+}\rangle + s[H_{-1}][R_m]|\mathbf{v}_{m1}^{2+}\rangle + s[H_{-1}][C_m]|\mathbf{v}_{m2}^{2+}\rangle \quad \text{for } |\mathbf{r}_2| < |s|, \quad m = -1. \quad (\text{A52})$$

Also from the definition of basis solutions in Eq. (4), we conclude that

$$|\mathbf{v}_{m2}^{1-}\rangle = [H_{-1}]|\mathbf{v}_{m2}^{2+}\rangle + s[H_{-1}][R_m]|\mathbf{v}_{m2}^{2+}\rangle - k^2s[H_{-1}][C_m]|\mathbf{v}_{m1}^{2+}\rangle \quad \text{for } |\mathbf{r}_2| < |s|, \quad m = -1. \quad (\text{A53})$$

At the same time, Eq. (A23) ensures that the derivative $(\frac{\partial}{\partial x} - i\frac{\partial}{\partial y})$ on both sides of Eq. (A42) renders the following relation:

$$|\psi_{(-1)}^{\text{PI-}}(\mathbf{r}_1)\rangle = [B^{\text{PI-}}][N_1^{\text{PI}}]^{-1}[N_2^{\text{PI}}][B^{\text{PI+}}]|\psi_{(-1)}^{\text{PI+}}(\mathbf{r}_2)\rangle. \quad (\text{A54})$$

Using Eq. (4), Eq. (A54) can be rewritten as

$$|\mathbf{v}_{m3}^{1-}\rangle = [P_{-1}]|\mathbf{v}_{m3}^{2+}\rangle \quad \text{for } |\mathbf{r}_2| < |s|, \quad m = -1, \quad (\text{A55})$$

where matrix $[P_{-1}]$ is defined as $[P_{-1}] = [B^{\text{PI-}}][N_1^{\text{PI}}]^{-1}[N_2^{\text{PI}}][B^{\text{PI+}}]$ as defined in Eq. (34). Finally, we combine Eqs. (A52), (A53), and (A55) to conclude

$$[M_{-1}^{12\mp}] = \begin{bmatrix} [H_{-1}] + s[H_{-1}][R_{-1}] & s[H_{-1}][C_{-1}] & 0 \\ -k^2s[H_{-1}][C_{-1}] & [H_{-1}] + s[H_{-1}][R_{-1}] & 0 \\ 0 & 0 & [P_{-1}] \end{bmatrix}, \quad (\text{A56})$$

where matrix $[M_{-1}^{12\mp}]$ expresses the transformation coefficients in Eq. (15) for $|\mathbf{r}_2| < |s|$, $m = m' = -1$. Matrix $[M_{-1}^{12\mp}]$ is identical to the one in Eq. (22) for $m = -1$. Submatrices $[R_{-1}]$ and $[C_{-1}]$ are defined in Eqs. (A10) and (A11) for $m = -1$, respectively.

-
- [1] H. Brinkman, A calculation of the viscous force exerted by a flowing fluid on a dense swarm of particles, *Flow, Turbul. Combust.* **1**, 27 (1949).
 - [2] S. Lee, S. U. S. Choi, and S. Li, Measuring thermal conductivity of fluids containing oxide nanoparticles, *J. Heat Trans.-Transact. Asme* **121**, 280 (1999).

- [3] J. A. Eastman, S. U. S. Choi, S. Li, W. Yu, and L. J. Thompson, Anomalous increased effective thermal conductivities of ethylene glycol-based nanofluids containing copper nanoparticles, *Appl. Phys. Lett.* **78**, 718 (2001).
- [4] K. Khanafer, K. Vafai, and M. Lightstone, Buoyancy-driven heat transfer enhancement in a two-dimensional enclosure utilizing nanofluids, *Int. J. Heat Mass Transfer* **46**, 3639 (2003).
- [5] D. T. Wasan and A. D. Nikolov, Spreading of nanofluids on solids, *Nature* **423**, 156 (2003).
- [6] T. G. Mason, Estimating the viscoelastic moduli of complex fluids using the generalized Stokes-Einstein equation, *Rheol. Acta.* **39**, 371 (2000).
- [7] C. Wilhelm, Out-of-Equilibrium Microrheology Inside Living Cells, *Phys. Rev. Lett.* **101**, 028101 (2008).
- [8] D. Wirtz, Particle-Tracking Microrheology of living cells: Principles and applications, *Ann. Rev. Biophys.* **38**, 301 (2009).
- [9] M. Parvazinia, V. Nassehi, R. Wakeman, and M. Ghoreishy, Finite element modeling of flow through a porous medium between two parallel plates using the brinkman equation, *Transp. Porous Media* **63**, 71 (2006).
- [10] L. Durlfolsky and J. Brady, Analysis of the brinkman equation as a model for flow in porous media, *Phys. Fluids* **30**, 3329 (1987).
- [11] M. Minale, Modelling the flow of a second order fluid through and over a porous medium using the volume averages. I. The generalized brinkman's equation, *Phys. Fluids* **28**, 023102 (2016).
- [12] W. C. Chew, Vector potential electromagnetics with generalized gauge for inhomogeneous media: Formulation, *Prog. Electromagnetics Res.* **149**, 69 (2014).
- [13] A. S. Sangani and G. B. Mo, An $O(N)$ algorithm for Stokes and Laplace interactions of particles, *Phys. Fluids* **8**, 1990 (1996).
- [14] L. Durlfolsky, J. F. Brady, and G. Bossis, Dynamic simulation of hydrodynamically interacting particles, *J. Fluid Mech.* **180**, 21 (1987).
- [15] A. J. C. Ladd, Hydrodynamic interactions in suspensions of spherical particles, *J. Chem. Phys.* **88**, 5051 (1988).
- [16] R. B. Jones, Spherical particle in Poiseuille flow between planar walls, *J. Chem. Phys.* **121**, 483 (2004).
- [17] S. Navardi and S. Bhattacharya, Axial pressure-difference between far-fields across a sphere in viscous flow bounded by a cylinder, *Phys. Fluid* **22**, 103305 (2010).
- [18] S. Navardi and S. Bhattacharya, Effect of confining conduit on effective viscosity of dilute colloidal suspension, *J. Chem. Phys.* **132**, 114114 (2010).
- [19] S. Navardi and S. Bhattacharya, General methodology to evaluate two-particle hydrodynamic friction inside cylinder-bound viscous fluid, *Comput. Fluids* **76**, 149 (2013).
- [20] S. Navardi, S. Bhattacharya, and H. Wu, Stokesian simulation of two unequal spheres in a pressure-driven flow through a cylinder, *Comput. Fluids* **121**, 145 (2015).
- [21] J. A. Eastman, S. Phillpot, and S. Choi, Thermal transport in nanofluids, *Annu. Rev. Mater. Res.* **34**, 219 (2004).
- [22] J. Bławdziewicz and S. Bhattacharya, Comment on Drift without flux: Brownian walker with a space-dependent diffusion coefficient, *Europhys. Lett.* **63**, 789 (2003).
- [23] S. Bhattacharya, D. Gurung, and S. Navardi, Radial distribution and axial dispersion of suspended particles inside a narrow cylinder due to mildly inertial flow, *Phys. Fluids* **25**, 033304 (2013).
- [24] L. Y. Chen, S. C. Ying, and T. Ala-Nissila, Finding transition paths and rate coefficients through accelerated Langevin dynamics, *Phys. Rev. E* **65**, 042101 (2002).
- [25] T. G. Mason and D. A. Weitz, Optical Measurements of Frequency-Dependent Linear Viscoelastic Moduli of Complex Fluids, *Phys. Rev. Lett.* **74**, 1250 (1995).
- [26] S. Bhattacharya, Cooperative motion of spheres arranged in periodic grids between two parallel walls, *J. Chem. Phys.* **128**, 074709 (2008).
- [27] L. De Ryck, J.-P. Groby, P. Leclaire, W. Lauriks, A. Wirgin, Z. E. A. Fellah, and C. Depollier, Acoustic wave propagation in a macroscopically inhomogeneous porous medium saturated by a fluid, *Appl. Phys. Lett.* **90**, 181901 (2007).
- [28] J. Rubinstein, Effective equations for flow in random porous media with a large number of scales, *J. Fluid Mech.* **170**, 379 (1986).

- [29] M. A. Spaid and F. R. Phelan, Lattice Boltzmann methods for modeling microscale flow in fibrous porous media, [Phys. Fluids](#) **9**, 2468 (1998).
- [30] N. S. Martys, Improved approximation of the Brinkman equation using a lattice Boltzmann method, [Phys. Fluids](#) **13**, 1807 (2001).
- [31] B. Cichocki and R. B. Jones, Image representation of a spherical particle near a hard wall, [Physica A](#) **258**, 273 (1998).
- [32] A. Sierou and J. F. Brady, Accelerated Stokesian dynamics simulations, [J. Fluid Mech.](#) **448**, 115 (2001).
- [33] A. J. Banchio and J. F. Brady, Accelerated Stokesian dynamics: Brownian motion, [J. Chem. Phys.](#) **118**, 10323 (2003).
- [34] B. U. Felderhof and R. B. Jones, Displacement theorems for spherical solutions of the linear Navier-Stokes equations, [J. Math. Phys.](#) **30**, 339 (1989).